Combined effect of Cu0 and oxygen vacancies in Cu-based zeolites enables highly efficient photo-Fenton-like performance for water purification

Wei Zhang, Lan Wang, Chen Hou, Zhiqiang Zhu, Eric Lichtfouse, Christos Trapalis, Chuanyi Wang

Environ. Sci.: Nano, 11, 2481-2493, 2024

https://doi.org/10.1039/d4en00181h

Combined effect of Cu^0 and oxygen vacancies in Cu-based zeolites enables highly efficient photo-Fenton-like performance for water purification†

Wei Zhang, [a] Lan Wang, *[a] Chen Hou,[a] Zhiqiang Zhu,[a] Eric Lichtfouse,*[b] Christos Trapalis[c] and Chuanyi Wang [a]

The Cu-based heterogeneous photo-Fenton-like process has emerged as a promising technology in wastewater treatment, but efficient light harvesting and sufficient utilization of photogenerated electrons are still core issues. Herein, a dual strategy was proposed to achieve the high-efficiency removal of refractory organic pollutants using a Cu-doped zeolite with Cu^0 and oxygen vacancies (Cu^0@CuZ) in the photo-Fenton-like reaction. This is the first time that such a strategy employing Cu-based zeolites has been used. Cu^0@CuZ can completely degrade 20 mg L^{-1} phenol within 15 min under visible-light irradiation, and the rate constant was 40, 55, and 65 times higher than Cu_2O, CuO, and Cu^0, respectively. Cu^0@CuZ also presented excellent degradation performance for other typical refractory organic pollutants, surpassing most of the reported Cu-based catalysts to date. This superior performance highly depends on oxygen vacancies (Vo) and plasmonic Cu nanoparticles. The introduction of Vo and the creation of the surface plasmon resonance effect greatly enhanced the visible-light harvesting ability of the catalyst. Impressively, Vo and Cu^0 nanoparticles served as dual-channels for efficient electron transfer by enriching and then transferring photogenerated electrons to Cu(II), greatly expediting the reduction of Cu(II) to Cu(I). The synergistic effects of the dual-channel electron transfer and light-harvesting ability achieved sustained Cu(II)/Cu(I) cycling, thereby promoting H_2O_2 activation to produce more active species for organic pollutant degradation. This work provides an ingenious strategy to rationally establish a high-efficiency photo-Fenton-like catalyst for water remediation.

Environmental significance

Refractory organic pollutants with high toxicities in wastewater, especially residual toxic organic pollutants, seriously endanger the human health and aquatic ecosystems. The Cu-based heterogeneous photo-Fenton-like process as a promising technology is an effective solution for wastewater remediation. Herein, we developed an environment-friendly Cu-based heterogeneous catalyst for the degradation of refractory organic pollutants. The coexistence of Cu^0 nanoparticles and oxygen vacancies boosted the visible light absorbability of the catalyst and served as electron transfer dual-channels to transfer more photogenerated electrons for Cu(II)/Cu(I) redox cycles, thereby greatly promoting H_2O_2 activation to produce reactive oxygen species. The catalyst showed exceptional proficiency in the photo-Fenton-like degradation of various organic pollutants, and their degradation pathway was also evaluated as a safe detoxification process, ensuring meaningful environmental impact. Moreover, the catalyst possessed a wide pH tolerance and trace Cu leaching, which is conducive for practical applications.

1. Introduction

The aggravation of water pollution caused by the rapid industrial and agricultural development poses tremendous underlying risks to humans and the ecosystems.[1,2] The Fenton process, as a common advanced oxidation process (AOP), has received extensive attention in the field of water treatment because of its advantage of producing strong oxidative hydroxyl radicals (·OH) through the reaction between Fe^{2+} and H_2O_2.[3–5] However, the large-scale applications of the Fenton process are usually limited by slow Fe^{3+}/Fe^{2+} redox cycles and a narrow pH

[a] School of Environmental Science and Engineering, Shaanxi University of Science and Technology, Xi'an 710021, P.R. China. E-mail: wanglan@sust.edu.cn

[b] State Key Laboratory of Multiphase Flow in Power Engineering, Xi'an Jiaotong University, Xi'an 710000, P.R. China. E-mail: eric.lichtfouse@icloud.com

[c] Institute of Nanoscience and Nanotechnology, NCSR "Demokritos", Agia Paraskevi 15341, Greece

† Electronic supplementary information (ESI) available. See DOI: https://doi.org/10.1039/d4en00181h

application range.[6,7] The Cu-based heterogeneous Fenton-like reaction has been considered as a good substitute for the conventional Fenton reaction in recent years because the reaction rate of H_2O_2 with Cu(I) is faster than that with Fe(II) over a wide pH range.[8,9] However, the low cycling efficiency of Cu(II)/Cu(I) is a rate-limiting step for the Cu-based Fenton-like reaction, which is a key bottleneck. Semiconductor-based photocatalysis can generate photogenerated electrons (e^-) to accelerate the conversion of Cu(II) to Cu(I) for H_2O_2 activation. Hence, combining photocatalysis with the Fenton reaction can enhance the production of reactive oxygen species (ROS) for organic pollutant degradation.[10] Unfortunately, it is still a great challenge to facilitate the effective utilization of solar energy and photogenerated charges for rapid Cu(II)/Cu(I) redox cycles.

Cu-based zeolites, primarily including CuO_x-loaded zeolites[11,12] and Cu-modified zeolites,[13,14] have great potential as heterogeneous Fenton-like catalysts owing to their large specific surface area and abundant pore, which can provide plentiful accessible active sites for the activation of H_2O_2, as well as the adsorption of pollutant molecules. Moreover, the incorporation of Cu into the cavities or frameworks of zeolites can decrease Cu ion leaching, leading to the high stability of the catalyst.[15] Particularly, the low valence unsaturated Cu(I), as a high-energy species, could be formed and stabilized in the zeolite frameworks, accompanying the generation of oxygen vacancies (Vo),[16–18] which is beneficial for the catalytic reaction compared with the conventional supported Cu catalysts.[19] Previous studies have demonstrated that Cu-based zeolite catalysts also have efficient photocatalytic performance for NO_x decomposition,[20] water splitting,[21] and dye degradation under UV light irradiation.[22] However, the poor visible-light harvesting capacity and the fast recombination of photogenerated carriers of these catalysts greatly inhibit the sufficient utilization of photogenerated electrons. In fact, the introduction of Vo can form a shallow impurity state in the band gap, which can boost the absorption of visible light by the catalyst. In addition, the Vo acts as photoinduced charge traps, promoting the separation of electrons and holes (h^+), while providing the electron transfer channels for electron migration.[23,24] Furthermore, Cu^0 nanoparticles (NPs) can extend the light absorption range of the photocatalyst to the visible-light region through its surface plasmon resonance effect.[25,26] More importantly, given the excellent electron storage capability and electron conductivity of Cu^0,[27] the photogenerated electrons could be also trapped by Cu^0 and then expeditiously transferred to other target electron acceptors. Inspired by the above discussion, a hypothesis is put forward. Considering the insufficient visible-light absorption and the rapid charge recombination of Cu-modified zeolites, it may be possible to incorporate Cu NPs and Vo onto Cu-modified zeolites to enhance light harvesting, and enable the fast separation and transfer of the photogenerated carrier charges for efficient Cu(II)/Cu(I) cycling.

Herein, a novel oxygen-vacancy-rich Cu-doped zeolite decorated with Cu^0 (named as Cu^0@CuZ) was fabricated through a facile hydrothermal route with a post-annealing treatment. The coexistence of Cu^0 NPs and Vo could not only boost the visible light absorbability, but also could act as electron transfer channels to drive the efficient transfer of more electrons for Cu(II)/Cu(I) redox cycles, thus synergistically leading to the greatly enhanced photo-Fenton-like activity. The photo-Fenton-like catalytic performance was evaluated by degradation of refractory organic pollutants, such as phenol, 4-chlorophenol, diclofenac, methylene blue and so on. Influences of the initial pH, H_2O_2 concentration, and catalyst dosage on the degradation of phenol over Cu^0@CuZ were systematically investigated, and the enhanced catalytic activity of Cu^0@CuZ has been achieved in comparison with these counterparts, including commercial CuO and Cu_2O nanoparticles, as well as Cu nanoparticles. This work opens a new avenue for developing high-performance catalysts for the photo-Fenton-like reaction in water purification.

2. Experimental

2.1 Preparation of catalysts

The catalysts were prepared as follows: first, $CuSO_4{\cdot}5H_2O$ and tetraethylenepentamine (TEPA) were dissolved in 2 mL deionized water as solution A. 2.8 mmol cetrimonium bromide (CTAB) was added into 2.35 mL NaOH solution. Then, 7.65 mL deionized water, 0.1 mmol sodium aluminate, and 0.83 mL hexamethyleneimine (HMI) were added to the above alkaline solution as solution B. Next, solutions A and B were mixed, and colloidal silica was added. Finally, the mixture solution was stirred for several hours, and then transferred into an autoclave and maintained at 150 °C for 3 d. The product was dried in an oven overnight. The obtained sample was the Cu-doped zeolite precursor containing Cu^0 nanoparticles and Cu_2O (denoted as Cu^0@CuZ-p). After that, the as-prepared sample was further calcined under a constant flow of nitrogen at 550 °C for 8 h to obtain the powder Cu^0@CuZ. For comparison, the sample without copper was prepared.

2.2 Photo-Fenton-like activity evaluation

The photo-Fenton-like performance activity evaluation of the catalysts was as follows: The catalyst was added to an organic pollutant solution, and stirred vigorously for 30 min in a dark box. The solution pH was adjusted using sulfuric acid and/or sodium hydroxide. Then, H_2O_2 was added to the above suspension and illumination (Xe lamp, $\lambda > 400$ nm) was initiated immediately. At predetermined intervals, 3 mL suspension sample was withdrawn with a syringe and filtered through a 0.22 μm filter. After that, $Na_2S_2O_3$ was added to quench the residual H_2O_2.

2.3 Materials and methods

More details about the materials, characterizations, analytic methods, and density functional theory (DFT) calculations can be found in the ESI.†

3. Results and discussion

3.1 Characterization of catalysts

The schematic synthesis process of the catalysts is shown in Fig. 1a. Firstly, the Cu-doped zeolite precursor containing Cu^0 and Cu_2O (Cu^0@CuZ-p) was synthesized using CTAB as structure-directing and reducing agents by hydrothermal method. Afterward, upon annealing in a N_2 atmosphere, Cu_2O existing on the external surface of Cu^0@CuZ-p was further converted Cu^0 NPs, while Cu(II) in zeolite frameworks was reduced to Cu(I) in a reducing atmosphere, accompanied by the generation of Vo. Finally, the well-defined composite structure of Cu^0@CuZ is achieved through the combination of metallic Cu NPs on the outer surface of the Cu-doped zeolite with abundant Vo. The crystal structure of the samples was characterized by X-ray diffraction (XRD). As can be seen from Fig. 1b and S1,† the XRD pattern of the sample without Cu confirmed the formation of the beta zeolite (β-zeolite), where the two characteristic peaks at 6.2° (d = 13.2 Å) and 22.2° (d = 3.8 Å) corresponded to the (101) and (302) reflections of the β-zeolite, respectively, which was consistent with the literature.[28,29] When Cu was introduced into the β-zeolite, the obtained Cu^0@CuZ-p exhibited new peaks at 43.3°, 50.4°, and 74.1°, corresponding to the (111), (200), and (220) reflections of Cu^0 (JCPDS No. 04-0836), respectively.[30] Another set of peaks at 36.5°, 42.3°, and 61.3° were detected, which was assigned to (111), (200), and (220) for Cu_2O (JCPDS No. 05-0667), respectively.[31] Suffering a further annealing treatment, for the as-obtained Cu^0@CuZ sample, the diffraction peaks of Cu_2O disappeared, while the diffraction peak intensity of Cu^0 increased, indicating that Cu_2O in the precursor was converted to Cu^0 by carbothermal reduction. Moreover, the original crystal form of zeolite in Cu^0@CuZ was well maintained, but the peak at 6.2° slightly shifted to higher angle, which is caused by the incorporation of Cu^{2+} into the frameworks of the zeolite.[32]

The morphology of Cu^0@CuZ was analysed by transmission electron microscopy (TEM). The TEM image of Cu^0@CuZ showed a nanosphere with a mean diameter of about 25 nm (Fig. 1c). The high-resolution TEM (HRTEM) image displayed a clear lattice fringe (Fig. 1d), representing good crystallinity of Cu^0@CuZ. An inset image in Fig. 1d showed a lattice fringe spacing of 0.209 nm for Cu^0 (111) and 0.38 nm for β-zeolite (302), which matched well with the XRD results. Energy dispersive spectrometer (EDS) analysis results suggest the existence of Al, O, Cu, Na, and Si elements in Cu^0@CuZ (Fig. 1e). The Fourier transform infrared spectroscopy (FTIR) spectrum of Cu^0@CuZ showed an additional band at approximately 1092 cm^{-1} assigned to the Si-O-Cu bond compared with β-zeolite (Fig. S2†), confirming the successful preparation of Cu^0@CuZ.[33] The specific surface areas of Cu^0@CuZ and β-zeolite (Fig. 1f and S3†) are 133.9 and 63.2 $m^2\ g^{-1}$, respectively, which shows that the introduction of the Cu species remarkably enlarged the specific surface area of the catalyst. Furthermore, the N_2 adsorption–desorption isotherm of Cu^0@CuZ showed a typical mesoporous structure, which was further verified by the corresponding pore size distribution with a narrow peak at about 11.6 nm. In addition, the pore volume of β-zeolite increased after introduction of the Cu species (Table S1†), which indicated that the addition of Cu increased the porosity of the catalyst. These features endow the catalyst with more active sites, which favours the effective H_2O_2 activation and removal of pollutants.

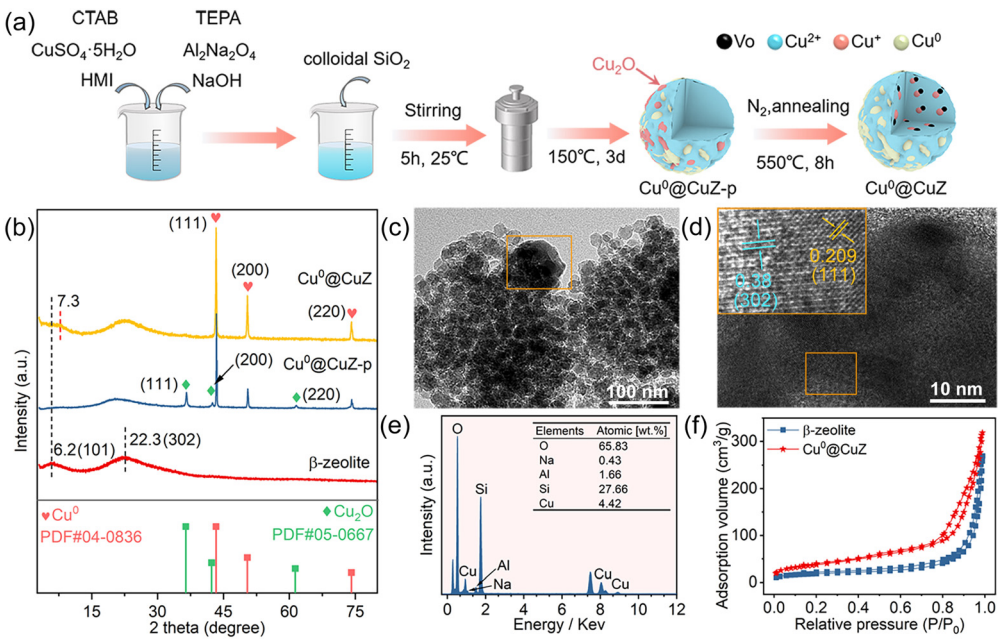

Fig. 1 (a) The synthesis process of the samples. (b) XRD patterns of the samples. (c) TEM and (d) HRTEM images of Cu^0@CuZ (inset of d: the fringe spacings correspond to β-zeolite and Cu^0). (e) EDS analysis of Cu^0@CuZ (inset of e: the relative elements content of Cu^0@CuZ). (f) Nitrogen adsorption–desorption isotherms of the samples.

X-ray photoelectron spectroscopy (XPS) was used to investigate the chemical composition and valence states of Cu^0@CuZ. The Al, O, Cu, Na, and Si elements were observed in Cu^0@CuZ *via* survey spectrum (Fig. S4†). The high-resolution Cu 2p spectrum (Fig. 2a) exhibited two peaks at 932.7 and 952.6 eV ascribed to the Cu $2p_{3/2}$ and Cu $2p_{1/2}$ orbitals of Cu^+/Cu^0, respectively, and another two peaks at 933.8 and 953.9 eV in the Cu 2p spectrum were assigned to Cu^{2+} $2p_{2/3}$ and Cu^{2+} $2p_{1/3}$, respectively.[34] Meanwhile, Cu Auger electron spectroscopy (AES) was further accurately used to distinguish between the Cu^+ and Cu^0 species. As displayed in Fig. 2b, the peaks at 569.51 eV and 572.98 eV were identified as Cu^0 and Cu^+, respectively,[35] which certifies that Cu^0 and Cu^+ coexist in Cu^0@CuZ. In fact, the coexistence of Cu^0 and Cu^+ favours the H_2O_2 activation in the Fenton-like reaction. Based on the deconvolution results, the calculated proportions of Cu^{2+}, Cu^+, and Cu^0 in Cu^0@CuZ were 34%, 24%, and 42%, respectively. Furthermore, the ratios of Cu^{2+}, Cu^+, and Cu^0 in Cu^0@CuZ-p were 37.2%, 29.8%, and 33%, respectively (Table S2†). Compared with Cu^0@CuZ-p, the increase of the Cu^0 proportion and decrease of the Cu(II) ratio in Cu^0@CuZ further confirmed that after calcination, Cu_2O on the external surface and Cu(II) in the zeolite frameworks of the precursor were reduced to Cu^0 and Cu(I), respectively. The O 1s spectrum of Cu^0@CuZ in Fig. 2c could be fitted into three peaks located at 530.7, 531.3, and 532.1 eV, which originated from the lattice oxygen, Vo, and hydroxyl species, respectively.[36] Additionally, it can be found that Cu^0@CuZ possessed the significant Vo peak (33.1%) compared with Cu^0@CuZ-p with a negligible Vo signal peak (3%), which verified that the reduction of Cu(II) to Cu(I) in the zeolite frameworks is accompanied by the formation of Vo. The Si 2p binding energy of 103.35 eV belongs to silicate.[37]

The solid-state electron paramagnetic resonance (EPR) spectra were used to detect unpaired electrons of the samples (Fig. 2d). An obvious EPR signal at g = 2.06 belonging to the Cu(II) (d^9) hyperfine coupling structure was observed in the Cu^0@CuZ-p spectrum, corroborating the existence of a large amount of Cu(II) in the β-zeolite lattice. By comparison, the Cu(II) signal was greatly weakened in Cu^0@CuZ, which is attributed to parts of Cu(II) being converted to EPR-silent Cu(I) during the carbothermal reduction process.[38] Previous studies have demonstrated that high temperature thermal treatment under N_2 atmosphere could achieve dehydration of the hydroxyl group and removal of the extra lattice O atoms, thus facilitating self-reduction of transition metals in zeolite. This would lead to the formation of low valence unsaturated Cu(I), accompanied with Vo.[16,18] As expected, a distinct Vo signal was detected at g = 2.007 in the Cu^0@CuZ spectrum.[39,40] By virtue of the XRD, XPS, and EPR results, we can conclude that different valence states of Cu species (Cu^{2+}, Cu^+, Cu^0) can be stably formed in the Vo-enriched zeolite, which is beneficial to the improvement of the photo-Fenton-like performance.

The light absorption characteristic of Cu^0@CuZ was recorded by UV-vis-DRS spectrum. As can be seen in Fig. 2e, Cu^0@CuZ exhibited absorption in the full spectrum region.

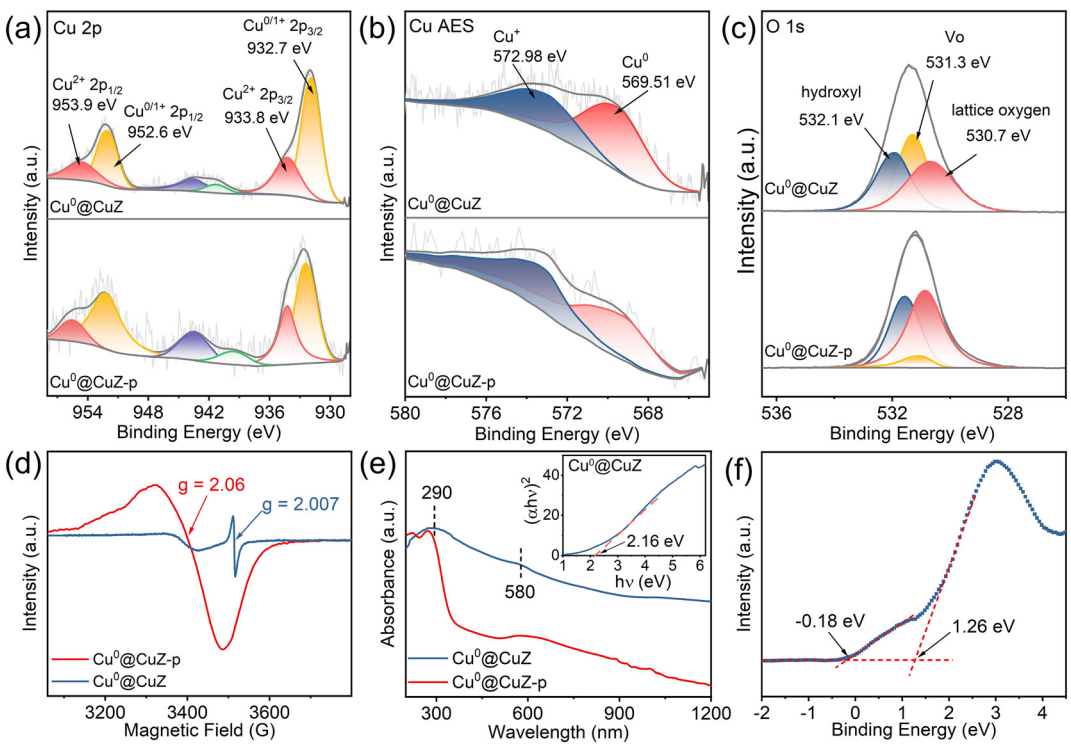

Fig. 2 (a) High-resolution XPS of Cu 2p, (b) Cu AES spectrum, and (c) high-resolution XPS of O 1 s for Cu^0@CuZ and Cu^0@CuZ-p. (d) Solid EPR spectra of samples. (e) UV-vis DRS spectrum (inset: band gap values) and (f) VB XPS spectrum of Cu^0@CuZ.

The intrinsic absorption at 200–400 nm was attributed to the charge-transfer transitions from oxygen to monomeric Cu^{2+} in the zeolite crystal lattice (Si–O–Cu),[41] and the absorption peak at 580 nm was ascribed to plasmon resonance of metallic Cu^0 NPs.[42] Additionally, the absorption at 600–900 nm can be attributed to the Vo defects and the d–d transition of Cu^{2+}.[43] Additionally, the Cu^0@CuZ shows a higher optical absorbance compared with Cu^0@CuZ-p. Thus, Cu^0@CuZ has a better light-harvesting ability in the visible region. Moreover, the optical band gap energy (E_g) of Cu^0@CuZ was estimated to be 2.16 eV based on the Kubelka–Munk transformation (eqn (1)),[44,45] where α, h, v, and A represent the absorption coefficient, Planck's constant, light frequency, and proportionality constant, respectively. The valence band (VB) value was determined to be 1.26 eV according to the VB XPS spectrum (Fig. 2f); therefore, the conduction band (CB) potential was −0.9 eV based on eqn (2). Moreover, an additional diffused electronic state, the VB tail state, was measured to be −0.18 eV in the VB XPS spectrum, which originates from the Vo defects. The VB tail would effectively reduce the energy required for the electronic transition, thereby enhancing the light absorption of the catalyst.[46,47] Conversely the E_g of Cu^0@CuZ-p was estimated to be 3.53 eV, which is much larger than that for Cu^0@CuZ (Fig. S5†), resulting in an increase in the energy required to generate photogenerated electron–hole pairs by excitation in visible light. The reduced band gap and increased visible light absorbability in Cu^0@CuZ are due to the present of oxygen vacancies and the increase of the plasmonic Cu^0 NPs content in Cu^0@CuZ. In summary, the coexistence of Cu^0 NPs and Vo intrinsically boosts the visible light absorbability of the catalyst.

$$\alpha h\nu = A(h\nu - E_g)^{1/2} \quad (1)$$

$$E_{VB} = E_{CB} + E_g \quad (2)$$

3.2 Photo-Fenton-like performance

The photo-Fenton-like performance of Cu^0@CuZ was investigated using phenol as a target pollutant. As depicted in Fig. 3a and S6a,† Cu^0@CuZ showed weak adsorption performance for phenol. Both visible/H_2O_2 and visible/Cu^0@CuZ systems exhibited inadequate oxidation capacity, and the phenol removal efficiency was less than 20%. In the presence of Cu^0@CuZ and H_2O_2 (Fenton-like system), the removal efficiency reached 50%, suggesting that Cu^0@CuZ possesses intrinsic Fenton-like activity, which can mainly be attributed to the fact that the Cu^+ originating from the zeolite lattice can activate H_2O_2 to produce ROS for phenol degradation. By contrast, the phenol removal efficiency was drastically elevated under the visible-light assistance. 100% of phenol was removed within 15 min in the Cu^0@CuZ photo-Fenton-like system. Furthermore, the corresponding rate constant (k) was calculated to be 0.387 min^{-1}, which was 16 times higher than that of the Fenton-like system (0.025 min^{-1}), indicating that the synergism of photocatalysis and the Fenton-like system can significantly boost the ROS generation. Moreover, Cu^0@CuZ showed better photo-Fenton-like

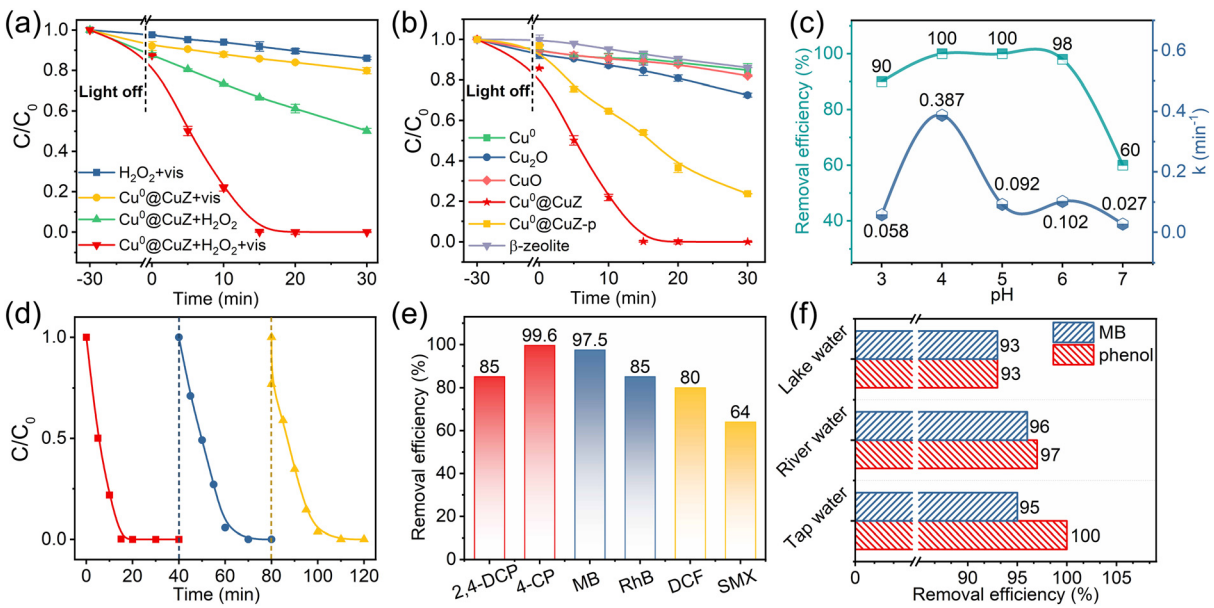

Fig. 3 Removal curves of phenol (a) under different conditions and (b) over different catalysts. (c) The removal efficiency of phenol over Cu^0@CuZ when the initial pH value was changed. (d) Reusability test of Cu^0@CuZ for phenol removal. (e) Removal efficiency of different pollutants over Cu^0@CuZ. (f) Removal efficiency of pollutants over Cu0@CuZ in different water samples. (Cu^0@CuZ: 0.2 g L^{-1}, H_2O_2: 10 mM, pH: 4, phenol: 20 mg L^{-1}, temperature: 25 °C, reaction time: 30 min; Cu^0: 9 mg L^{-1}, CuO: 11.25 mg L^{-1}, and Cu_2O: 10.14 mg L^{-1} were added to the solution to achieve the same Cu concentration of 9 mg L^{-1}).

performance for the removal of organic pollutants than some previously reported catalysts (Table S3†).

Furthermore, the phenol degradation over other catalysts, including commercial Cu_2O, CuO, Cu^0, as-prepared β-zeolite, and Cu^0@CuZ-p, was compared under the same photo-Fenton-like reaction conditions. As seen from Fig. 3b and S6b,† the phenol removal efficiency of the photo-Fenton-like process with CuO, Cu^0, or β-zeolite was close to the value observed in the vis/H_2O_2 system, indicating that these catalysts showed negligible catalytic activity towards H_2O_2 activation ability. The β-zeolite has no Fenton activity since β-zeolite is not equipped with the Cu active site that triggers the Fenton reaction. When Cu_2O was present in the photo-Fenton-like system, the phenol removal efficiency increased to 25%, which is due to the contribution of the Cu(I) sites in Cu_2O. Obviously, Cu^0@CuZ displayed a much higher phenol removal efficiency, and the corresponding k value was roughly 40, 55, 65, and 77 times higher than that of Cu_2O (0.01 min^{-1}), CuO (0.007 min^{-1}), Cu^0 (0.006 min^{-1}), and β-zeolite (0.05 min^{-1}), respectively. Moreover, Cu^0@CuZ showed a higher phenol removal efficiency than Cu^0@CuZ-p at 15 min. The excellent catalytic performance of Cu^0@CuZ can be attributed to the following aspects. For one thing, the Cu^+ species in the zeolite frameworks are capable to react with H_2O_2 to produce ·OH. In addition, the surface plasmon resonance effect of Cu^0 NPs and the shallow impurity level of Vo augment the visible-light harvesting ability of Cu^0@CuZ. Hence, a large number of photogenerated charge carriers are generated. Meanwhile, the Vo and Cu^0 as electron transfer dual-channels can capture the photogenerated electrons, and then transfer them to the adjacent Cu(II). This accelerated the Cu(II)/Cu(I) redox cycles, which boosted the H_2O_2 activation to generate ROS. Alternately, to confirm that the presence of Vo and Cu^0 provided electrons for the reduction of Cu(II) to Cu(I) in Cu^0@CuZ, we measured the high-resolution XPS of Cu 2p and Cu AES spectrum of Cu^0@CuZ after 30 min irradiation, and compared them with Cu^0@CuZ-p (Fig. S7 and Table S2†). After 30 min of visible-light irradiation, the proportions of the Cu species in Cu^0@CuZ-p did not change significantly. Meanwhile, the Cu^+ proportion increased from 24% to 29.5%, and the Cu^{2+} proportion decreased from 34% to 29.4% in Cu^0@CuZ, confirming that the photogenerated electrons were transferred to the Cu(II) site by Vo and Cu^0 for Cu(II) reduction. In brief, the combined action of Cu(I), Cu^0, and Vo is conducive to improving the ROS generation and achieving the superior photo-Fenton-like performance.

The effect of reaction parameters (*e.g.*, initial pH, H_2O_2 concentration, and catalyst dosage) on the removal efficiency of phenol over Cu^0@CuZ was systematically studied. As shown in Fig. 3c, the phenol removal efficiency was more than 90% within 30 min when the initial pH was less than 6, indicating that Cu^0@CuZ has a wider pH application range compared with traditional Fenton catalysts. Generally speaking, an initial pH of 2–3 is beneficial for the traditional Fenton reaction. Additionally, the highest k value was obtained when the initial pH was 4. Thus, pH 4 was selected for subsequent experiments. Moreover, the optimized 10 mM H_2O_2 concentration and 0.2 g L^{-1} of catalyst dosage were selected as the reaction parameters (Fig. S8†). The effects of coexisting anions (Fig. S9†) on the phenol removal efficiency showed that the addition of CO_3^{2-} inhibited the phenol removal efficiency by 63%, which is due to the quenching effects of CO_3^{2-} on ·OH (eqn (3)).[48] The reusability of Cu^0@CuZ is also a crucial factor to evaluate its catalytic performance. As displayed in Fig. 3d, the phenol removal efficiency over Cu^0@CuZ still reached 100% within 120 min after three consecutive cycles. Furthermore, the leaching amount of Cu ions is 1.5 mg L^{-1}. This value is lower than the wastewater discharging standard in the European Union (2 mg L^{-1}),[49] suggesting the excellent structure stability of Cu^0@CuZ. In addition, the XPS spectra of the used catalyst showed negligible changes compared with the fresh catalyst (Fig. S4†), further demonstrating that Cu^0@CuZ has good chemical stability.

$$CO_3^{2-} + \cdot OH \rightarrow \cdot CO_3^{-} + OH \quad (3)$$

The universal applicability of Cu^0@CuZ was further investigated using environment-related refractory organic pollutants, including 2,4-dichlorophenol (2,4-DCP), 4-chlorophenol (4-CP), methylene blue (MB), rhodamine B (RhB), diclofenac (DCF), and sulfamethoxazole (SMX). All of the selected pollutants were well degraded (Fig. 3e). Meanwhile, the mineralization ability of Cu^0@CuZ for pollutants was evaluated by total organic carbon (TOC). The TOC removal rate of phenol and MB was 70.5% and 48%, respectively, after 90 min in the photo-Fenton-like system (Fig. S10†). Moreover, we further investigated the treatment effect of Cu^0@CuZ on complex actual waters (*e.g.*, lake water, river water, and tap water) supplemented with 20 mg L^{-1} phenol or MB (Fig. 3f and S11†). Notably, Cu^0@CuZ still exhibited high removal efficiency for these organic pollutants in natural waters, highlighting the practicability of Cu^0@CuZ in water treatment. The long-term treatment of phenol by the continuous flow photo-Fenton reactor was also performed to evaluate the practical application of Cu^0@CuZ. As is shown in Fig. 4, the H_2O_2 solution and the phenol solution with catalyst were respectively pumped into the continuous flow reactor to trigger the photo-Fenton-like reaction under visible light irradiation. It is evident that more than 90% phenol could be removed after continuous operation for 400 min, reflecting the superior durability and catalytic activity of Cu^0@CuZ.

3.3 Mechanism analysis

To further understand the mechanism of Cu^0@CuZ in the photo-Fenton-like reaction, active species scavenging experiments and EPR tests were carried out.[50] Five scavengers, including *t*-Butyl alcohol (TBA), benzoquinone (BQ), histidine, silver nitrate ($AgNO_3$), and KI, were used to trap ·OH, $\cdot O_2^-$, $^1O_2$, e^-, and h^+, respectively. As shown in Fig. 5a, the phenol removal was distinctly inhibited with the addition of TBA, BQ, histidine,

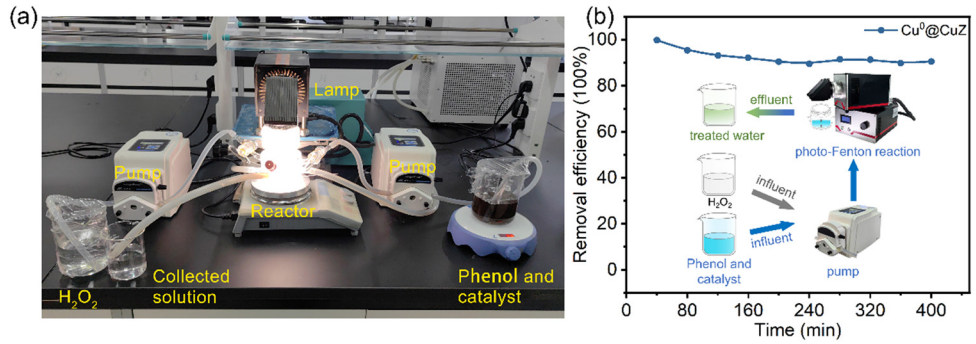

Fig. 4 (a) Picture of the continuous flow reactor. (b) The removal efficiency of phenol over Cu^0@CuZ by the continuous flow photo-Fenton reactor (inset: diagram of the continuous flow reactor).

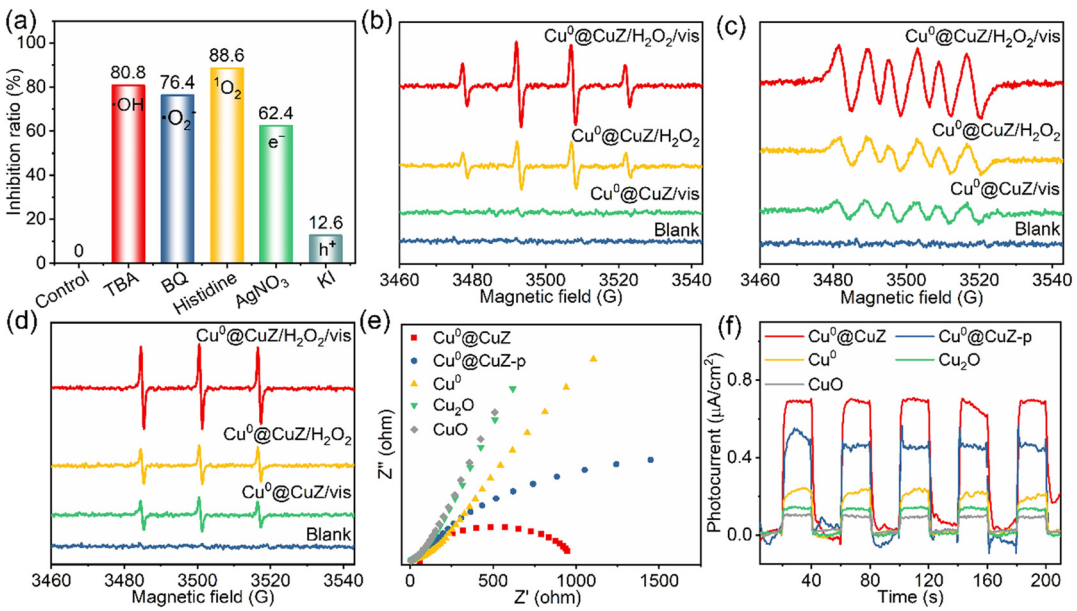

Fig. 5 (a) Effects of the addition of different scavengers on the removal of phenol. EPR spectra of (b) DMPO–·OH, (c) DMPO–$·O_2^-$, and (d) TEMP–$^1O_2$ in various systems (the blank represents the solution containing DMPO/TEMP without the catalyst). (e) Electrochemical impedance spectroscopy (EIS) and (f) transient photocurrent response of the samples.

and $AgNO_3$ into the reaction system, suggesting that ·OH, $·O_2^-$, $^1O_2$, and e^- made primary contributions for the phenol degradation. Additionally, the phenol removal efficiency was inhibited by 12.6% with the addition of KI, indicating that h^+ played a secondary role therein. Furthermore, DMPO and 4-oxo-TEMP were used as spin traps combined with EPR technique to detect the participation of ROS in the pollutant degradation and explore the synergistic effect among Cu^0@CuZ, H_2O_2, and visible light (Fig. 5b–d). The DMPO–·OH signal in the Cu^0@CuZ/vis system was negligible. Furthermore, the Cu^0@CuZ/H_2O_2 system exhibited distinct DMPO–·OH characteristic peaks. After the visible-light irradiation, the DMPO–·OH signal was significantly enhanced in the Cu^0@CuZ/H_2O_2/vis system. Moreover, the DMPO–$·O_2^-$ signal was detected in the Cu^0@CuZ/vis system, verifying that photogenerated electrons can reduce O_2 to produce $·O_2^-$. The Cu^0@CuZ/H_2O_2 system also showed a similar $·O_2^-$ signal, while a stronger $·O_2^-$ signal was present in the Cu^0@CuZ/H_2O_2/vis system. The variation trend of the TEMP-$^1O_2$ signal was the same as that of DMPO–$·O_2^-$, which verified that $^1O_2$ could be produced by the conversion of radicals. The above results directly corroborate that the synergistic effect between photocatalysis and the Fenton-like system can vastly boost the ROS generation.

The charge separation and transfer of the catalysts were also investigated by the transient photocurrent response and electrochemical impedance spectroscopy (EIS). The relative size of the arc radius on the Nyquist plot corresponds to the charge transfer resistance and the separation efficiency of the photogenerated carriers. In comparison, Cu^0@CuZ exhibited the significantly smallest arc radius (Fig. 5e), showing that the coexistence of Vo and Cu^0 could substantially reduce the charge transfer resistance and improve the conductivity, resulting in

faster photogenerated electron transfer. The photocurrent density–time (*I*–*t*) curves of the samples were tested under the visible-light irradiation. As seen from Fig. 5f, Cu^0@CuZ exhibited a higher photocurrent density of 0.69 μA cm^{-2}, which is approximately 3, 5, and 7 times higher than that of the Cu^0 (0.24 μA cm^{-2}), Cu_2O (0.14 μA cm^{-2}), and CuO (0.1 μA cm^{-2}), indicating that Cu^0@CuZ can produce more photogenerated charge carriers and realize efficient photogenerated charge separation. Moreover, the photocurrent density of Cu^0@CuZ is higher than that of Cu^0@CuZ-p, further confirming that the combined effect of Vo and Cu^0 is advantageous to the separation of the photogenerated charge. The above results directly infer that the electron transfer dual-channels formed by Vo and Cu^0 NPs drive the efficient transfer of more electrons, achieving advantageous electron transport for the Cu(II)/Cu(I) redox cycles to activate H_2O_2.

The possible mechanism of the Cu^0@CuZ composite as a heterogeneous photo-Fenton-like catalyst for the organic pollutant removal is proposed based on the above experiments and discussion (Fig. 6). Specifically, when H_2O_2 was added to the suspension, the Fenton-like reaction occurred. First, the Cu^0@CuZ can catalyze H_2O_2 activation to produce ROS, in which the electron-rich Cu^+ in the zeolite lattice plays a major role (eqn (4) and (5)). Then, when Cu^0@CuZ was exposed to visible-light, the photogenerated electrons were excited to the VB tail and further leaped to CB, while leaving h^+ in VB. A part of the photogenerated electrons would react with O_2 to produce $\cdot O_2^-$. Another part of the photogenerated electrons was trapped by Cu^0 and Vo to reduce Cu(II) to Cu(I), thereby accelerating the Cu(II)/Cu(I) cycling and promoting the H_2O_2 activation for the generation of ROS (eqn (6)–(8)). The boosted Cu(II)/Cu(I) cycling is essential for Cu^0@CuZ to maintain excellent photo-Fenton-like performance. The $^1O_2$ can be produced by disproportionation and the Haber–Weiss reaction between radicals (eqn (9)–(11)).[51,52] Additionally, the h^+ could directly decompose a small amount of pollutants (eqn (12)).[53] Finally, these ROS attacked organic pollutant molecules to break them down into CO_2 and H_2O (eqn (13)).

$$Cu^+ + H_2O_2 \rightarrow Cu^{2+} + \cdot OH + OH^- \quad (4)$$

$$Cu^{2+} + H_2O_2 \rightarrow Cu^+ + \cdot HO_2 + H^+ \quad (5)$$

$$Cu^0@CuZ + h\nu \rightarrow e^- + h^+ \quad (6)$$

$$Cu^{2+} + e^- \underset{Vo}{\overset{Cu^0}{\rightarrow}} Cu^+ \quad (7)$$

$$O_2 + e^- \rightarrow \cdot O_2^- \quad (8)$$

$$2\cdot O_2^- + 2H^+ \rightarrow {}^1O_2 + H_2O_2 \quad (9)$$

$$\cdot OH + \cdot O_2^- \rightarrow {}^1O_2 + OH^- \quad (10)$$

$$4\cdot OH + \rightarrow {}^1O_2 + H_2O \quad (11)$$

$$h^+ + \text{pollutants} \rightarrow \text{intermediates} \quad (12)$$

$$\cdot OH/\cdot O_2/{}^1O_2/h^+ + \text{pollutants} \rightarrow H_2O + CO_2 \quad (13)$$

3.4 DFT calculations and toxicity assessment

DCF, which has a relatively large molecular mass, the highest predicted environmental risk, and high toxicity among environment-related refractory organic pollutants, was selected as the model pollutant for DFT calculations, liquid chromatograph-mass spectrometer (LC-MS) analysis, and

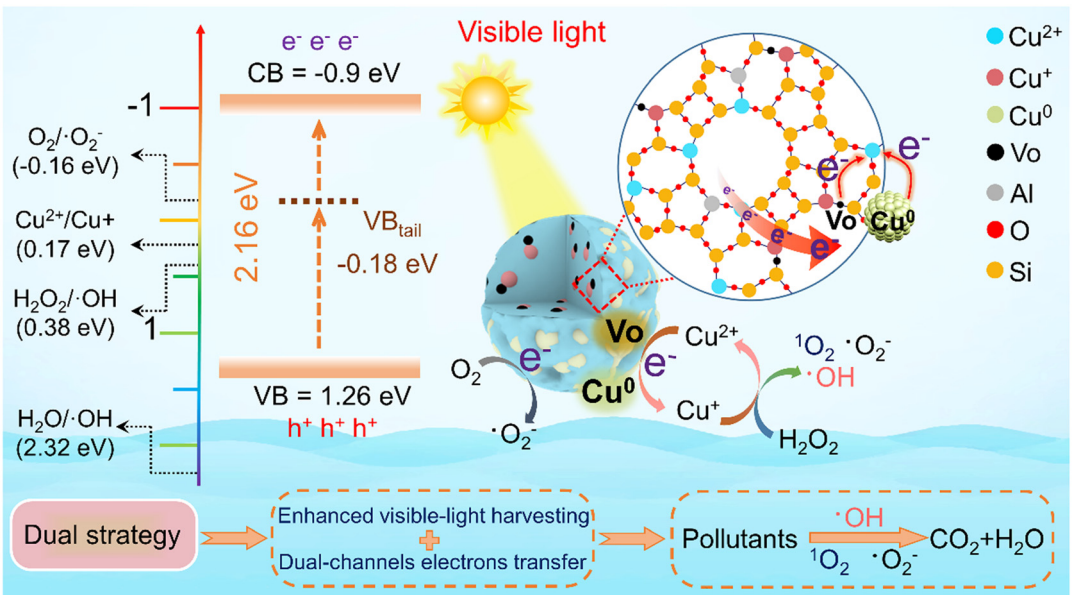

Fig. 6 Mechanism diagram of pollutant degradation over Cu^0@CuZ in the photo-Fenton-like system.

toxicity assessment to assess the detoxifying performance of Cu^0@CuZ to organic pollutants. The optimized molecular structure of DCF is illustrated in Fig. 7a. The highest occupied molecular orbital (HOMO) was liable to lose electrons and undergo electrophilic reactions, while the lowest unoccupied molecular orbital (LUMO) is apt to gain electrons and occur nucleophilic reactions (Fig. 7b and c). However, these cannot accurately express the sites of the electrophilic radical attack on DCF.[54,55] In order to exactly predict the reaction site of the DCF attack by radicals, the electrostatic potential (ESP) and Fukui function of DCF were further calculated.[56] In the ESP mapping (Fig. 7d), the electron-rich region was shown in blue with a negative electrostatic potential and called as electrophilic sites, while the electron-deficient region was shown in red with a positive electrostatic potential and regarded as nucleophilic sites. For DCF, there are more negative electrostatic potentials near the O28, N12, Cl10, and C5 sites, suggesting that these sites held higher electrophilic reactivity and were more prone to electron transfer. The Fukui index (Fig. 7e) was used to precisely predict the radical attack sites of DCF, in which the higher Fukui indices (f^0) of C1 (0.067), C2 (0.0554), C5 (0.0478), Cl10 (0.0807), Cl11 (0.0563), N12 (0.0587) C175 (0.0412), and C20 (0.067) indicate them as vulnerable sites to radical attack.

Based on the LC-MS (Fig. S12†) and DFT calculations results, we propose the following possible degradation pathway (Fig. 8a), including ring closure, cleavage of C–N bond, and hydroxylation.[57] Firstly, the Cl10 atom of DCF was lost under the attack by ·OH or $\cdot O_2^-$, accompanied by structural rearrangement to form the intermediate B (m/z = 259). Further dechlorination, ring-opening, and subsequent oxidation led to the gradual decomposition of intermediate B to generate products C–G. Secondly, the N atom was easily attacked, resulting in cleavage of the C–N bond of DCF, followed by deethylation to form the small molecule H (m/z = 162), which then gradually broke down into smaller molecules under radical attack. The presence of the main intermediate quinone imine, which would have been formed from C1 or C20 atoms attacked by radicals through the hydroxylation reaction, was not detected. This is possibly

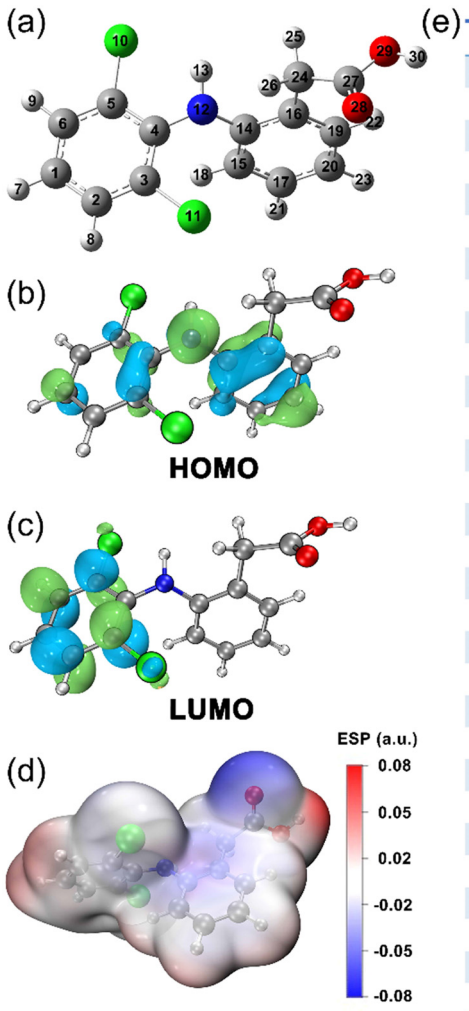

(e)

Atom	q(N)	q(N+1)	q(N-1)	f^-	f^+	f^0
1(C)	-0.0404	-0.1115	0.0224	0.0628	0.0712	0.067
2(C)	-0.0451	-0.1274	-0.0166	0.0285	0.0823	0.0554
3(C)	0.0164	-0.0057	0.0413	0.0249	0.0221	0.0235
4(C)	0.0338	-0.014	0.0478	0.0141	0.0478	0.0309
5(C)	0.0095	-0.0575	0.0381	0.0286	0.067	0.0478
6(C)	-0.047	-0.0871	-0.0156	0.0314	0.0401	0.0358
7(H)	0.0531	0.0149	0.083	0.0299	0.0382	0.0341
8(H)	0.0521	0.012	0.0748	0.0227	0.0401	0.0314
9(H)	0.0525	0.0234	0.0763	0.0238	0.029	0.0264
10(Cl)	-0.0413	-0.1333	0.028	0.0694	0.0919	0.0807
11(Cl)	-0.0284	-0.0883	0.0243	0.0527	0.0598	0.0563
12(N)	-0.0992	-0.1114	0.006	0.1052	0.0122	0.0587
13(H)	0.1075	0.0912	0.1381	0.0306	0.0164	0.0235
14(C)	0.0344	0.0119	0.0693	0.0349	0.0225	0.0287
15(C)	-0.06	-0.073	-0.02	0.04	0.013	0.0265
16(C)	-0.0084	-0.0387	0.0326	0.041	0.0304	0.0357
17(C)	-0.0414	-0.083	-0.0005	0.0409	0.0415	0.0412
18(H)	0.0368	0.0296	0.0562	0.0194	0.0072	0.0133
19(C)	-0.046	-0.0717	-0.0112	0.0349	0.0257	0.0303
20(C)	-0.049	-0.1026	0.0315	0.0805	0.0535	0.067
21(H)	0.0461	0.0211	0.0748	0.0287	0.025	0.0269
22(H)	0.0363	0.0177	0.0607	0.0244	0.0186	0.0215
23(H)	0.0444	0.0147	0.0803	0.0359	0.0297	0.0328
24(C)	-0.0508	-0.0603	-0.042	0.0088	0.0095	0.0091
25(H)	0.0433	0.024	0.0621	0.0188	0.0194	0.0191
26(H)	0.0429	0.0365	0.0509	0.008	0.0064	0.0072
27(C)	0.2126	0.1954	0.2172	0.0046	0.0172	0.0109
28(O)	-0.2742	-0.3048	-0.2477	0.0265	0.0306	0.0285
29(O)	-0.1753	-0.1902	-0.1631	0.0122	0.0149	0.0135
30(H)	0.185	0.1682	0.2008	0.0158	0.0168	0.0163

Fig. 7 (a) Optimized DCF molecular structure. (b) HOMO and (c) LUMO orbitals of DCF. (d) Electrostatic potential (ESP) mapping of the molecular surface of DCF. (e) Fukui index of DCF.

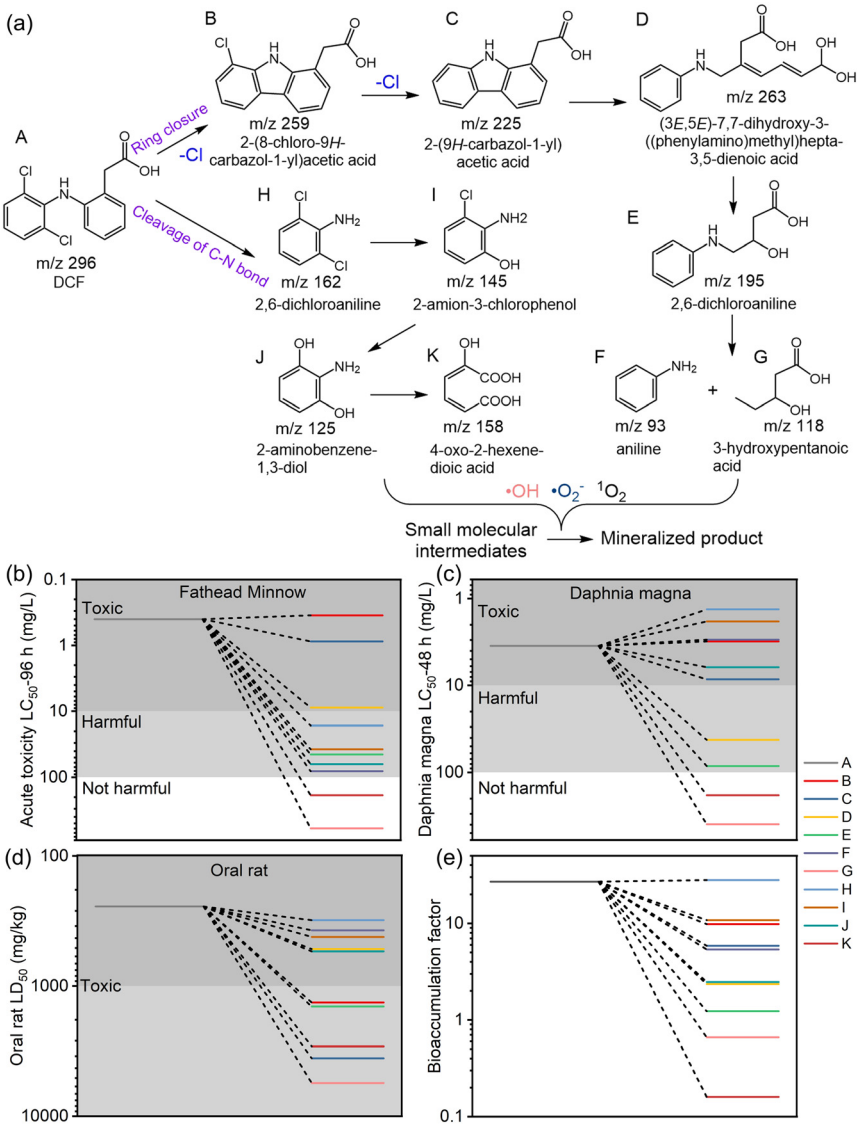

Fig. 8 (a) The degradation pathway of DCF over Cu^0@CuZ. (b) Fathead minnow LC_{50}-96 h, (c) *Daphnia magna* LC_{50}, (d) oral rat LD_{50}, and (e) bioaccumulation factor of DCF and its degradation intermediates.

because the quinone imine was rapidly broken down. Finally, with the increase of ROS attacking, all of the above intermediates converted to CO_2 and H_2O.

The toxicity of the DCF degradation intermediates was evaluated by the toxicity estimation software tool (T.E.S.T), including the fathead minnow LC_{50}-96 h, *Daphnia magna* LC_{50}-48 h, oral rat LD_{50}, and bioaccumulation factor.[58] Fig. 8b shows the reduced fathead minnow LC_{50}-96 h value of all degradation intermediates except product B, and products G and K even became no longer harmful after further decomposition. The *Daphnia magna* LC_{50}-48 h value (Fig. 8c) of most intermediates was also reduced. Moreover, as shown in Fig. 8d, the oral rat LD_{50} of DCF is 244.02 mg kg^{-1}, and the higher LD_{50} value signifies the lower toxicity. Notably, all of the intermediates had higher oral rat LD_{50} values than DCF, indicating reduced toxicity of these intermediates. Similarly, the bioaccumulation factors (Fig. 8e) of the intermediates B to K were all smaller than those of DCF, specifying that the bioaccumulation effect could also be cut down by the photo-Fenton-like reaction. In summary, the Cu^0@CuZ photo-Fenton-like system can significantly reduce the toxicity of organic pollutants and their intermediates.

Conclusion

In conclusion, we developed a novel oxygen-vacancy-rich Cu-doped zeolite decorated with Cu^0 and Vo through a facile hydrothermal route with a post-annealing treatment. The experimental results showed that the Cu^0 NPs (accounts for about 40% of the total copper content) and the abundant Vo defects greatly enhanced the visible-light harvesting ability of the catalyst. Additionally, the Vo defects and Cu^0 NPs served as

electron transfer dual-channels to improve the transfer efficiency of photogenerated electrons through enriching and migrating them to Cu(II) sites. Eventually, the combined effect of Cu^0 and Vo greatly expedited the reduction of Cu(II) to Cu(I) and improved the activation of H_2O_2, facilitating the enhanced photo-Fenton-like activity. As expected, Cu^0@CuZ displayed excellent removal efficiency for phenols, antibiotics, and dyes in the heterogeneous photo-Fenton-like system, showing better photo-Fenton-like performance than some previously reported Cu-based catalysts. The TOC removal rate of phenol reached 71% with 90 min. EPR results showed that ·OH, $\cdot O_2^-$, and $^1O_2$ made major contributions for the pollutants degradation. Meanwhile, Cu^0@CuZ had a wide pH tolerance and excellent reusability. Furthermore, the experiments on the removal of organic pollutants in complex actual waters over Cu^0@CuZ highlighted the catalyst's universal practicability in water treatment. Notably, Cu^0@CuZ photo-Fenton-like system can significantly reduce the toxicity of the degradation intermediates. Overall, this study proposes a facile strategy to achieve the sustained Cu(II)/Cu(I) redox cycles for H_2O_2 activation, paving new ways to design cost-effective catalysts for water remediation.

Author contributions

Wei Zhang: conceptualization, formal analysis, investigation, data curation, writing – original draft, writing – review & editing. Lan Wang: project administration, resources, supervision, writing – review & editing. Chen Hou: data curation. Zhiqiang Zhu: validation. Eric Lichtfouse: supervision, writing – review & editing. Christos Trapalis: supervision. Chuanyi Wang: supervision.

Conflicts of interest

The authors declare that there are no conflicts to declare.

Acknowledgements

This work was supported by the National Natural Science Foundation of China (grant no. 22076114), the Key Research and Development Program of Shaanxi (2021SF-452), and the "Thousand Talents Program" of Shaanxi province of China is gratefully acknowledged.

References

1 S. Fang, W. Zhang, K. Sun and Y. H. Hu, Highly efficient thermo-photocatalytic degradation of tetracycline catalyzed by tungsten disulfide under visible light, *Environ. Chem. Lett.*, 2022, **21**, 1287–1295.

2 T. Liu, S. Xiao, N. Li, J. Chen, X. Zhou, Y. Qian, C. H. Huang and Y. Zhang, Water decontamination via nonradical process by nanoconfined Fenton-like catalysts, *Nat. Commun.*, 2023, **14**, 2881.

3 J. Zhang, Y. Wang, B. Peng, S. Wen and Q. Zhang, Light-induced degradation of organic pollutants under high salinity conditions using titanium dioxide/ferrocene polymer nanocomposites as photocatalyst and H_2O_2 activator simultaneously, *Environ. Sci.: Nano*, 2024, **11**, 431–440.

4 P. Jiang, T. Zhou, J. Bai, Y. Zhang, J. Li, C. Zhou and B. Zhou, Nitrogen-containing wastewater fuel cells for total nitrogen removal and energy recovery based on Cl·/ClO·oxidation of ammonia nitrogen, *Water Res.*, 2023, **235**, 119914.

5 Z. Yang, Z. Wang, J. Wang, Y. Li and G. Zhang, Facet-dependent activation of oxalic acid over magnetic recyclable Fe_3S_4 for efficient pollutant removal under visible light irradiation: Enhanced catalytic activity, DFT calculations, and mechanism insight, *Environ. Sci. Technol.*, 2022, **56**, 18008.

6 Z. Yang, A. Yu, C. Shan, G. Gao and B. Pan, Enhanced Fe(III)-mediated Fenton oxidation of atrazine in the presence of functionalized multi-walled carbon nanotubes, *Water Res.*, 2018, **137**, 37–46.

7 W. Hu, M. Yang, Q. Yan, J. Ji, Y. Bao, J. Zhang and M. Xing, Defect electrons accelerate iron cycle of novel Fe-based Fenton: Long-term effective quinoline degradation, *Chin. Chem. Lett.*, 2023, **34**, 108109.

8 G. Subramanian and H. Prakash, Photo augmented copper-based fenton disinfection under visible LED light and natural sunlight irradiation, *Water Res.*, 2021, **190**, 116719.

9 Z. Zhu, L. Wang, W. Zhang, C. Hou, C. Wang and J. Zhao, Ultrathin $CuNi_2Al$-LDH nanosheets with enhanced electron transfer for visible-light-driven photo-fenton-like water decontamination, *Chem. Eng. J.*, 2024, **481**, 148313.

10 R. Liu, Y. Xu and B. Chen, Self-assembled nano-FeO(OH)/reduced graphene oxide aerogel as a reusable catalyst for photo-Fenton degradation of phenolic organics, *Environ. Sci. Technol.*, 2018, **52**, 7043–7053.

11 L.-L. Lou and S. Liu, CuO-containing MCM-48 as catalysts for phenol hydroxylation, *Catal. Commun.*, 2005, **6**, 762–765.

12 K. M. Parida and D. Rath, Surface characterization and catalytic evaluation of copper-promoted Al-MCM-41 toward hydroxylation of phenol, *J. Colloid Interface Sci.*, 2009, **340**, 209–217.

13 X. Zhou, H. Chen, X. Cui, Z. Hua, Y. Chen, Y. Zhu, Y. Song, Y. Gong and J. Shi, A facile one-pot synthesis of hierarchically porous Cu(I)-ZSM-5 for radicals-involved oxidation of cyclohexane, *Appl. Catal., A*, 2013, **451**, 112–119.

14 L. Singh, P. Rekha and S. Chand, Cu-impregnated zeolite Y as highly active and stable heterogeneous Fenton-like catalyst for degradation of Congo red dye, *Sep. Purif. Technol.*, 2016, **170**, 321–336.

15 Z. Shangguan, X. Yuan, L. Jiang, Y. Zhao, L. Qin, X. Zhou, Y. Wu, J. W. Chew and H. Wang, Zeolite-based Fenton-like catalysis for pollutant removal and reclamation from wastewater, *Chin. Chem. Lett.*, 2022, **33**, 4719–4731.

16 P. J. Smeets, J. S. Woertink, B. F. Sels, E. I. Solomon and R. A. Schoonheydt, Transition-metal ions in zeolites: coordination and activation of oxygen, *Inorg. Chem.*, 2010, **49**, 3573–3583.

17 A. Mech, A. Monguzzi, F. Cucinotta, F. Meinardi, J. Mezyk, L. De Cola and R. Tubino, White light excitation of the near infrared Er^{3+} emission in exchanged zeolite sensitised by

oxygen vacancies, *Phys. Chem. Chem. Phys.*, 2011, **13**, 5605–5609.
18 Y. Wang, H. Li, L. Gu, Q. Gan, Y. Li and G. Calzaferri, Thermally stable luminescent lanthanide complexes in zeolite L, *Microporous Mesoporous Mater.*, 2009, **121**, 1–6.
19 J. Yang, M. Zhang, M. Chen, Y. Zhou and M. Zhu, Oxygen vacancies in piezoelectric ZnO twin-mesocrystal to improve peroxymonosulfate utilization efficiency via piezo-activation for antibiotic ornidazole removal, *Adv. Mater.*, 2023, **35**, e2209885.
20 M. Matsuoka and M. Anpo, Local structures, excited states, and photocatalytic reactivities of highly dispersed catalysts constructed within zeolites, *J. Photochem. Photobiol., C*, 2003, **3**, 225–252.
21 J. Lu, D. Zhang, H. Lin, R. Hong, C. Tao, Z. Han and S. Zhuang, Photocatalytic water splitting properties of Cu^{2+} exchanged Beta zeolites, *Nanotechnology*, 2020, **31**, 145715.
22 A. Nezamzadeh-Ejhieh and S. Hushmandrad, Solar photodecolorization of methylene blue by CuO/X zeolite as a heterogeneous catalyst, *Appl. Catal., A*, 2010, **388**, 149–159.
23 L. Hao, H. Huang, Y. Zhang and T. Ma, Oxygen vacant semiconductor photocatalysts, *Adv. Funct. Mater.*, 2021, **31**, 2100919.
24 H. Li, J. Li, Z. Ai, F. Jia and L. Zhang, Oxygen vacancy-mediated photocatalysis of BiOCl: Reactivity, selectivity, and perspectives, *Angew. Chem., Int. Ed.*, 2018, **57**, 122–138.
25 J. Li, Z. Lou and B. Li, Nanostructured materials with localized surface plasmon resonance for photocatalysis, *Chin. Chem. Lett.*, 2022, **33**, 1154–1168.
26 M. Sayed, J. Yu, G. Liu and M. Jaroniec, Non-noble plasmonic metal-based photocatalysts, *Chem. Rev.*, 2022, **122**, 10484–10537.
27 Y. Deng, C. Wan, C. Li, Y. Wang, X. Mu, W. Liu, Y. Huang, P. K. Wong and L. Ye, Synergy effect between facet and zero-valent copper for selectivity photocatalytic methane formation from CO_2, *ACS Catal.*, 2022, **12**, 4526–4533.
28 Q. Wu, X. Wang, G. Qi, Q. Guo, S. Pan, X. Meng, J. Xu, F. Deng, F. Fan, Z. Feng, C. Li, S. Maurer, U. Muller and F. S. Xiao, Sustainable synthesis of zeolites without addition of both organotemplates and solvents, *J. Am. Chem. Soc.*, 2014, **136**, 4019–4025.
29 Y. Yue, X. Guo, T. Liu, H. Liu, T. Wang, P. Yuan, H. Zhu, Z. Bai and X. Bao, Template free synthesis of hierarchical porous zeolite Beta with natural kaolin clay as alumina source, *Microporous Mesoporous Mater.*, 2020, **293**, 109772–109779.
30 H. Shi, Y. T. Zhou, R. Q. Yao, W. B. Wan, X. Ge, W. Zhang, Z. Wen, X. Y. Lang, W. T. Zheng and Q. Jiang, Spontaneously separated intermetallic Co_3Mo from nanoporous copper as versatile electrocatalysts for highly efficient water splitting, *Nat. Commun.*, 2020, **11**, 2940.
31 P. Shen, B. Zhou, Z. Chen, W. Xiao, Y. Fu, J. Wan, Z. Wu and L. Wang, Ruthenium-doped 3D Cu_2O nanochains as efficient electrocatalyst towards hydrogen evolution and hydrazine oxidation, *Appl. Catal., B*, 2023, **325**, 122305.
32 Z. He, J. Wu, B. Gao and H. He, Hydrothermal synthesis and characterization of aluminum-free Mn-beta zeolite: a catalyst for phenol hydroxylation, *ACS Appl. Mater. Interfaces*, 2015, **7**, 2424–2432.
33 A. Corma, V. Fornes, S. B. Pergher, T. L. M. Maesen and J. G. Buglass, Delaminated zeolite precursors as selective acidic catalysts, *Nature*, 1998, **396**, 353–356.
34 T. Guo, L. Jiang, H. Huang, Y. Li, X. Wu and G. Zhang, Enhanced degradation of tetracycline in water over Cu-doped hematite nanoplates by peroxymonosulfate activation under visible light irradiation, *J. Hazard. Mater.*, 2021, **416**, 125838.
35 Y. Wang, W. Zhou, R. Jia, Y. Yu and B. Zhang, Unveiling the activity origin of a copper-based electrocatalyst for selective nitrate reduction to ammonia, *Angew. Chem., Int. Ed.*, 2020, **59**, 5350–5354.
36 S. Yao, A. Zhang, Z. Liu, Y. Li, Y. Fu and W. Chi, Biomass-assisted synthesis of long-rod TiO_2 with oxygen vacancies active sites and biomass carbon for efficient photocatalytic reduction of Cr(VI) under visible light, *Surf. Interfaces*, 2024, **46**, 104110.
37 L. Wang, D. W. Bahnemann, L. Bian, G. Dong, J. Zhao and C. Wang, Two-dimensional layered zinc silicate nanosheets with excellent photocatalytic performance for organic pollutant degradation and CO_2 conversion, *Angew. Chem., Int. Ed.*, 2019, **58**, 8103–8108.
38 W. Cai, M. Gu, W. Jin and J. Zhou, CTAB-functionalized C@SiO_2 double-shelled hollow microspheres with enhanced and selective adsorption performance for Cr(VI), *J. Alloys Compd.*, 2019, **777**, 1304–1312.
39 T. Zhou, L. Li, J. Li, J. Wang, J. Bai, L. Xia, Q. Xu and B. Zhou, Electrochemically reduced TiO_2 photoanode coupled with oxygen vacancy-rich carbon quantum dots for synergistically improving photoelectrochemical performance, *Chem. Eng. J.*, 2021, **425**, 131770.
40 T. Zhou, J. Wang, Y. Zhang, C. Zhou, J. Bai, J. Li and B. Zhou, Oxygen vacancy-abundant carbon quantum dots as superfast hole transport channel for vastly improving surface charge transfer efficiency of $BiVO_4$ photoanode, *Chem. Eng. J.*, 2022, **431**, 133414.
41 M. Rutkowska, U. Díaz, A. E. Palomares and L. Chmielarz, Cu and Fe modified derivatives of 2D MWW-type zeolites (MCM-22, ITQ-2 and MCM-36) as new catalysts for DeNOx process, *Appl. Catal., B*, 2015, **168–169**, 531–539.
42 Y. Sun, P. Tian, D. Ding, Z. Yang, W. Wang, H. Xin, J. Xu and Y.-F. Han, Revealing the active species of Cu-based catalysts for heterogeneous Fenton reaction, *Appl. Catal., B*, 2019, **258**, 117985.
43 T. Čižmar, I. Panžić, I. Capan and A. Gajović, Nanostructured TiO_2 photocatalyst modified with Cu for improved imidacloprid degradation, *Appl. Surf. Sci.*, 2021, **569**, 151026.
44 T. Zhou, J. Wang, S. Chen, J. Bai, J. Li, Y. Zhang, L. Li, L. Xia, M. Rahim, Q. Xu and B. Zhou, Bird-nest structured ZnO/TiO_2 as a direct Z-scheme photoanode with enhanced light harvesting and carriers kinetics for highly efficient and stable photoelectrochemical water splitting, *Appl. Catal., B*, 2020, **267**, 118599.
45 T. Zhou, S. Chen, J. Wang, Y. Zhang, J. Li, J. Bai and B. Zhou, Dramatically enhanced solar-driven water splitting of

$BiVO_4$ photoanode via strengthening hole transfer and light harvesting by co-modification of CQDs and ultrathin β-FeOOH layers, *Chem. Eng. J.*, 2021, **403**, 126350.

46 X. Chen, L. Liu, P. Y. Yu and S. S. Mao, Increasing solar absorption for photocatalysis with black hydrogenated titanium dioxide nanocrystals, *Science*, 2011, **331**, 746–750.

47 H. Wang, H. Ma, Y. Li, L. Cheng, J. Yang and J. Liu, Facile synthesis of TiO_2 with a narrow bandgap and low valence band for efficient visible-light photocatalytic degradation of various phenols, *Ind. Eng. Chem. Res.*, 2023, **62**, 14320–14334.

48 C. Hou, L. Wang, W. Zhang, Z. Zhu, S. Lu, F. Zou and C. Wang, Construction of TiO_{2-x} confined by layered iron silicate toward efficient visible-light-driven photocatalysis-Fenton synergistic removal of organic pollutants, *ACS Appl. Mater. Interfaces*, 2023, **15**, 23124–23135.

49 H. Liang, R. Liu, X. An, C. Hu, X. Zhang and H. Liu, Bimetal-organic Frameworks with coordinatively unsaturated metal sites for highly efficient Fenton-like catalysis, *Chem. Eng. J.*, 2021, **414**, 128669.

50 M. Zhang, W. Guo, Y. Chen, D. He, A. B. Isaev and M. Zhu, Dissolved oxygen in aeration-driven piezo-catalytic for antibiotics pollutants removal in water, *Chin. Chem. Lett.*, 2023, **34**, 108229.

51 Y. Li, X. Wang, Z. Duan, D. Yu, Q. Wang, D. Ji and W. Liu, Zn/Co-ZIFs@MIL-101(Fe) metal-organic frameworks are effective photo-Fenton catalysts for RhB removal, *Sep. Purif. Technol.*, 2022, **293**, 121099.

52 M. Liu, H. Xia, W. Yang, X. Liu, J. Xiang, X. Wang, L. Hu and F. Lu, Novel Cu-Fe bi-metal oxide quantum dots coupled g-C_3N_4 nanosheets with H_2O_2 adsorption-activation trade-off for efficient photo-Fenton catalysis, *Appl. Catal., B*, 2022, **301**, 120765.

53 Y. Xiang, Y. Huang, B. Xiao, X. Wu and G. Zhang, Magnetic yolk-shell structure of $ZnFe_2O_4$ nanoparticles for enhanced visible light photo-Fenton degradation towards antibiotics and mechanism study, *Appl. Surf. Sci.*, 2020, **513**, 145820.

54 C. Zhao, J. Wang, X. Chen, Z. Wang, H. Ji, L. Chen, W. Liu and C. C. Wang, Bifunctional $Bi_{12}O_{17}Cl_2$/MIL-100(Fe) composites toward photocatalytic Cr(VI) sequestration and activation of persulfate for bisphenol A degradation, *Sci. Total Environ.*, 2021, **752**, 141901.

55 Z. Yang, Y. Li, X. Wang, J. Li, J. Wang and G. Zhang, Facet-dependent activation of oxalic acid over hematite nanocrystals under the irradiation of visible light for efficient degradation of pollutants, *J. Environ. Sci.*, 2024, **142**, 204.

56 Y. Li, Y. Yang, J. Lei, W. Liu, M. Tong and J. Liang, The degradation pathways of carbamazepine in advanced oxidation process: A mini review coupled with DFT calculation, *Sci. Total Environ.*, 2021, **779**, 146498.

57 W. Liu, Y. Li, F. Liu, W. Jiang, D. Zhang and J. Liang, Visible-light-driven photocatalytic degradation of diclofenac by carbon quantum dots modified porous g-C_3N_4: Mechanisms, degradation pathway and DFT calculation, *Water Res.*, 2019, **151**, 8–19.

58 X. Huo, H. Yi, E. Almatrafi, D. Ma, Y. Fu, L. Qin, W. Xia, L. Xiang, F. Xu, H. Yan, C. Zhou, G. Zeng and C. Lai, Insights into Fenton-like oxidation of oxytetracycline mediated by Fe-doped porous g-C_3N_4 nanomaterials: synthesis, performance and mechanism, *Environ. Sci.: Nano*, 2023, **10**, 1828–1841.

Supplementary Information

Combined effect of Cu^0 and oxygen vacancy in Cu-based zeolite enables highly efficient photo-Fenton-like performance for water purification

Wei Zhang, [a] Lan Wang *[a], Chen Hou [a], Zhiqiang Zhu [a], Eric Lichtfouse *[b], Christos Trapalis [c], and Chuanyi Wang [a]

[a] *School of Environmental Science and Engineering, Shaanxi University of Science and Technology, Xi'an 710021, PR China*

[b] *State Key Laboratory of Multiphase Flow in Power Engineering, Xi'an Jiaotong University, Xi'an 710000, PR China*

[c] *Institute of Nanoscience and Nanotechnology, NCSR "Demokritos", Agia Paraskevi 15341, Greece*

* Corresponding author.

E-mail addresses: wanglan@sust.edu.cn; eric.lichtfouse@icloud.com

1. Texts

Text S1. Materials.

Sodium aluminate ($Al_2O_3 \cdot Na_2O$, 98%), Cetrimonium bromide (CTAB, 99%), Sodium hydroxide (NaOH, 98%), Hexamethyleneimine (HMI, 98%), Tetraethylenepentamine (TEPA, 98%), Sodium thiosulfate ($Na_2S_2O_3$, 99%) and Sodium carbonate (Na_2CO_3, 99.8%) were purchased from Aladdin Co., Ltd.. LUDOX AS-40 colloidal silica (40 wt%), Copper (II) sulfate pentahydrate ($CuSO_4 \cdot 5H_2O$, 99%), benzoquinone (BQ, 99%), L-Histidine (99%), and tert-Butanol (TBA, 99%) were purchased from Merck Co., Ltd.. Phenol (99%), 2,4−Dichlorophenol, 4−chlorophenol (Sigma-Aldrich Co., Ltd.). Hydrogen peroxide, Sulfuric acid (Sinopharm Chemical Reagent Co., Ltd.). Silver nitrate (Tianjin Tiangan Chemical Technology Development Co., Ltd.). All reagents were not purified. Deionized water was prepared by pure water meter and was used throughout the experiment.

Text S2. Characterization.

XRD patterns was recorded from 3° to 80° with nickel-filtered Cu Kα radiation (λ = 1.54 Å Rigaku, Smart Lab 9kW). Operating conditions: voltage is 45 kV, scanning rate is 10°/min. TEM was carried out using FEI Talos F200x Microscope, which operating voltage is 200kv. EDS elemental analysis was conducted using Bruker X-Flash SDD 5010. XPS was performed on Thermo SCIENTIFIC K-Alpha spectrometer (Al Kαlph source). The specific surface areas were measured by a surface area analyzer (ASAP2460, Micromeritics, USA) with the Brunauer-Emmett-Teller (BET) method, and the pore size distribution was calculated using BJH calculations method. DRS spectroscopy measurement was recorded on a spectrophotometer (Agilent-Cary 5000, USA) from 200 nm to 1200 nm. FTIR spectra were recorded on a Bruker Vertex70 (4000−400 cm^{-1}). EIS was measure on CHI 660E (Chenhua Co., Ltd., China). The copper leaching during the reaction was measured by an ICP-AES (Thermo Scientific, ICAP 6300 Duo) instrument.

Text S3. Analytic methods.

The degradation was monitored via high performance liquid chromatograph (Ultimate 3000, Thermo Fisher Scientific) with a DAD-300 detector, C18 Hypersil GOLD column at column chamber temperature of 35 °C. The test conditions are as follows: phenol (60% H_2O, 40% methanol, flow rate:

1 mL/min, UV: 283 nm). 4−CP (30% H_2O, 70% methanol, flow rate: 1 mL/min, UV: 224 nm). 2.4−DCP (70% acetonitrile, 30% H_2O, UV: 286 nm). DCF (35% acetic acid aqueous solution (0.1%), 65% acetonitrile, UV: 274 nm). MB and RhB were detected by ultraviolet spectrophotometer.

In addition, EPR was used to detect the involved reaction ROS, 5,5-Dimethyl-1-pyrroline n-oxide (DMPO) was dispersed in different air-saturated methanol and aqueous dispersions. A 300 W Xe lamp ($\lambda > 400$ nm) was used as a visible-light source. In the absence of H_2O_2, a total of 100 μL of DMPO (176.75 mM) was added into 100 μL of the prepared degradation solution (water for •OH, methyl alcohol for $\bullet O_2^-$, 0.2 g/L catalyst, 10 mM H_2O_2, pH 4). Then, the mixed solution was held for 5 min under light. The solution was sucked out by a quartz capillary tube with an inner diameter of 1 mm, and the spectrum was recorded by placing the capillary tube in the EPR cavity. For comparison, H_2O_2 (10 mM) was added into solution before light irradiation to detect the different signals, and other conditions keep constant. The preparation of 2,2,6,6-tetramethyl-4-oxo-piperidine (4-oxo-TEMP) solution is the same as DMPO. 20 mg sample was placed into the sample tube and then into the ESR cavity to detect oxygen vacancy.

TOC of initial and irradiated samples were measured on Elementar TOC analyzer. For EIS test, the ITO glass coating with catalyst was used as a working electrode, and using Pt sheet and Ag/AgCl served as the counter and the reference electrode, respectively. The electrolyte solution: 0.1 M Na_2SO_4.

Text S4. DFT calculations

Gaussian09, D01 software package was used to DFT calculations[1]. We used the B3LYP functional and 6-31G(d) basis (Grimme dispersion corrections, GD3BJ) to optimize the model of pollutants. Then, the singlet point energy calculations were based on the B3LYP functional and a larger 6-311G(d) basis. The Hirshfeld atomic charges, HOMO/LUMO gap, ESP and Fukui functions were achieved with the help of the Multiwfn program[2, 3].Fukui function has been widely used to predict reactive sites of electrophilic, nucleophilic, and radical attacking[4].

2. Table

Table S1. Specific surface area (S_{BET}), pore size (d) and pore volume (Vt) of the samples.

sample	Structural parameters		
	$S_{BET}(m^2/g)$	d(nm)	$V_t(cm^3/g)$
β-zeolite	63.2	27.99	0.41
Cu^0@CuZ	133.9	14.81	0.48

Table S2 The Cu content of Cu^0@CuZ-P and Cu^0@CuZ.

Catalyst	Cu^0 content (%)	Cu^+ content (%)	Cu^{2+} content (%)
Cu^0@CuZ-p	33	29.8	37.2
Cu^0@CuZ	42	24	34
Cu^0@CuZ-p after illumination	33.7	29.6	36.7
Cu^0@CuZ after illumination	41.1	29.5	29.4

Table S3. Degradation conditions and pollutants removal efficiency over Cu^0@CuZ and other catalysts.

target pollutants	catalysts	reaction conditions	catalytic performance	references
phenol	$FeOOH/Bi_2MoO_6$	pH: 3.0; catalyst: 1.0 g/L; $[H_2O_2]$: 20 mM; C_0: 5 mg/L; T: 25 °C	100% removal in 3 h, k = 1.13876 h^{-1}	[5]
phenol	Fe_3O_4-GO	pH: 5.0; catalyst: 0.25 g/L; $[H_2O_2]$: 10 mM; C_0: 20 mg/L; T: 25 °C	100% removal after 120 min, k = –	[6]
phenol	FeOOH quantum dots coupled to g-C_3N_4	pH: 5.0; catalyst: 4 g/L; $[H_2O_2]$: 20 mM; C_0: 50 mg/L; T: 25 °C	100% removal after 90 min, k = 0.054 min^{-1}	[7]
phenol	Cu-iminodisuccinic acid complex	pH: 7.0; catalyst: 0.02 mM; $[H_2O_2]$: 14.7 mM; C_0: 50 mg/L; T: 25 °C	95% removal after 60 min, k = –	[8]
phenol	AG/Fe_3O_4	pH: 7.0; catalyst: 0.5 mg/L; $[H_2O_2]$: 250 mM; C_0: 40 mg/L; T: 25 °C	100% removal after 120 min, k = 0.02083 min^{-1}	[9]
4-CP	$La_{1-x}Ti_xFeO_3$	pH: 3.0; catalyst: 0.5 g/L; $[H_2O_2]$: 3.7 mM; C_0: 25 mg/L; T: 25 °C	100% removal in 200 min, k = 0.0025 min^{-1}	[10]
MB	MA-Cu-Fe@C	pH: 5; catalyst: 0.5 g/L; $[H_2O_2]$: 32 mM; C_0: 50 mg/L; T: 25 °C	98.8% removal after 80 min, k = 0.054 min^{-1}	[11]
RhB	Zn/Co-ZIFs@MIL-101(Fe)	pH: 5; catalyst: 0.2 g/L; $[H_2O_2]$: 90 mM; C_0: 100 mg/L; T: 25 °C	98% removal after 3 h, k = 1.33 h^{-1}	[12]
TC	CuFeO QDs/CNNSs	pH: 6; catalyst: 0.5 g/L; $[H_2O_2]$: 100 mM; C_0: 50 mg/L; T: 25 °C	100% removal in 25 min, k = –	[13]
phenol/MB		pH: 4.0; catalyst: 0.2 g/L; $[H_2O_2]$: 10.0 mM; C_0: 20 mg/L; T: 25 °C	100% removal in 20 min, k = 0.387 min^{-1}	this work

3. Figures

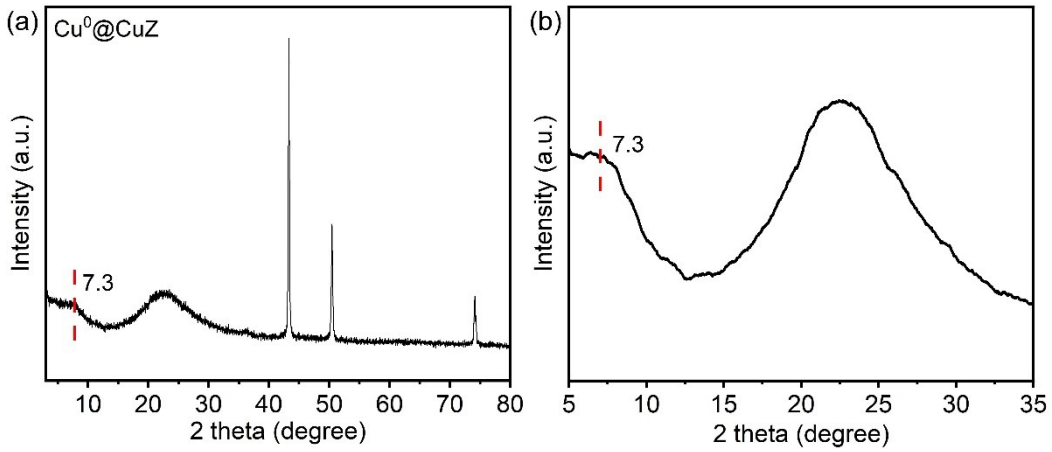

Fig. S1 (a) XRD pattern of Cu^0@CuZ. (b) Enlarged view of the XRD pattern of Cu^0@CuZ.

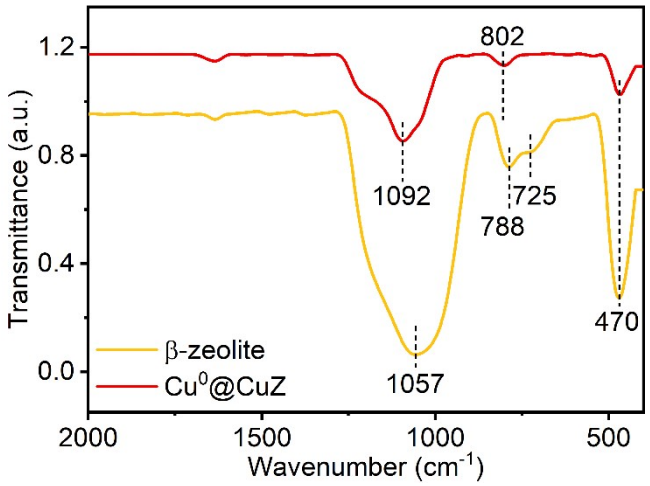

Fig. S2 FTIR spectra of samples.

The FTIR spectrum showed that bands around 470, 725, 788, 1057 cm^{-1} were characterized to β-zeolite. By contrast, an additional band at approximately 1092 cm^{-1} was assigned to Si-O-Cu bond compared with β-zeolite [14-16].

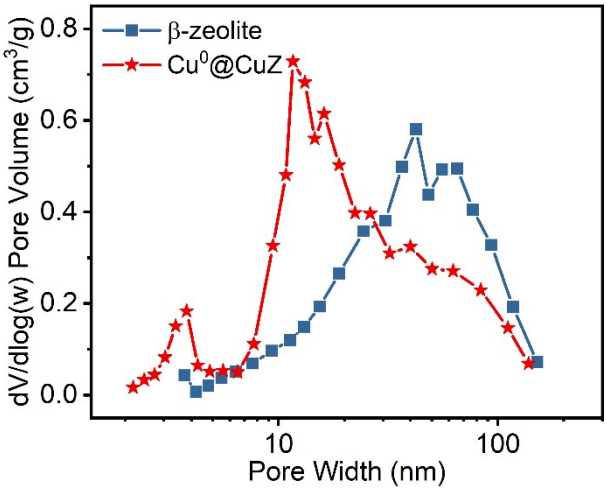

Fig. S3 Pore size distribution of Cu^0@CuZ and β-zeolite.

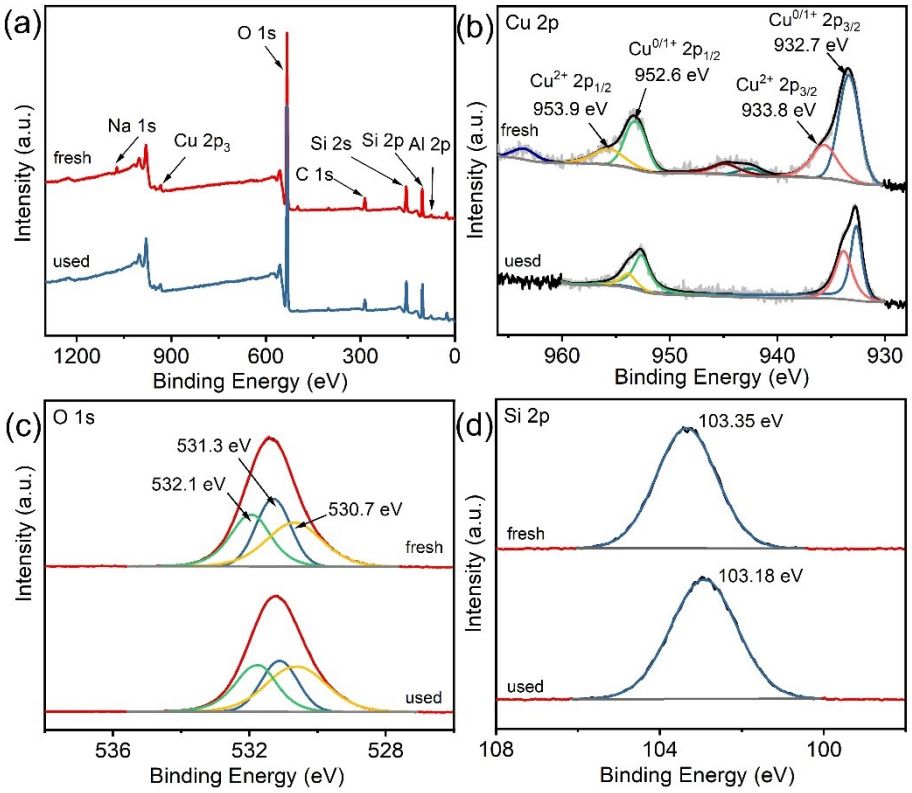

Fig. S4 (a) Wide scan XPS spectrum of Cu^0@CuZ. High-resolution XPS spectra of (b) Cu 2p, (c) O 1s and (d) Si 2p for Cu^0@CuZ.

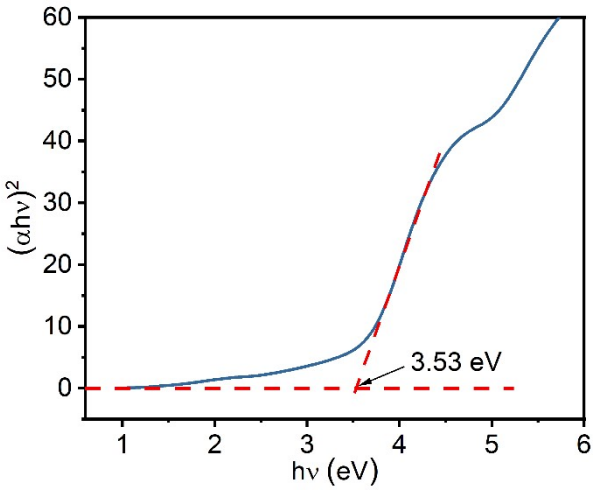

Fig. S5 Band gap values of Cu^0@CuZ-p.

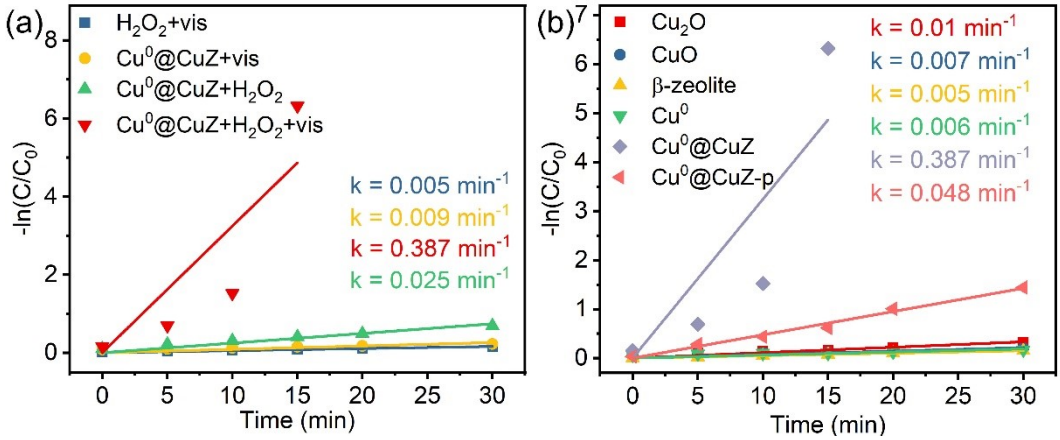

Fig. S6 (a) *k* values of various reaction systems. (b) *k* values over different catalysts in the photo-Fenton-like system.

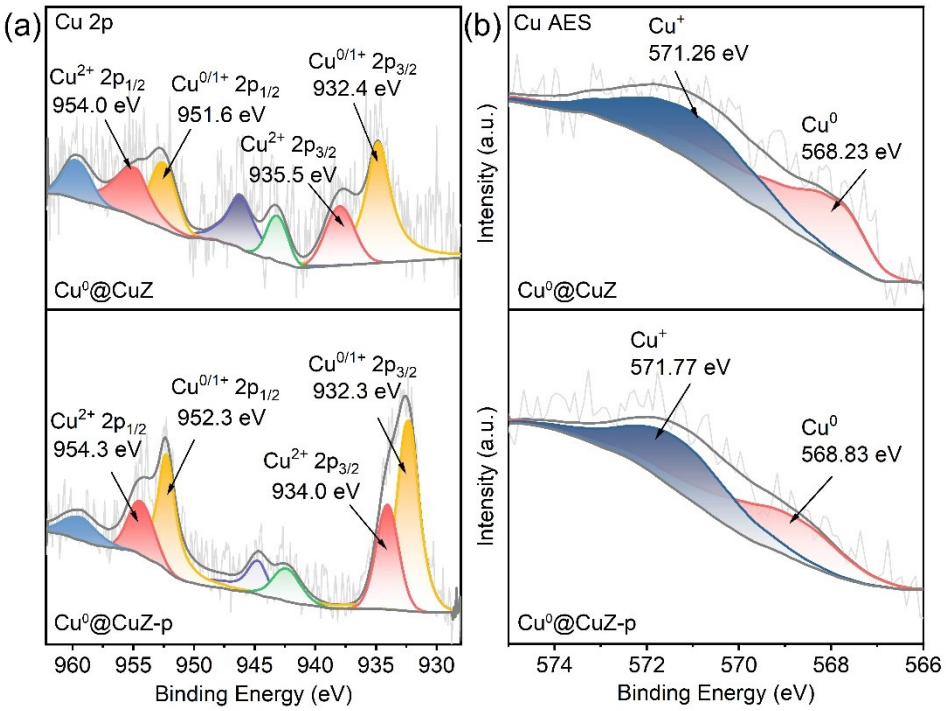

Fig. S7 The high-resolution XPS of Cu 2p and Cu AES spectrum of Cu^0@CuZ and Cu^0@CuZ-p after 30 min illumination.

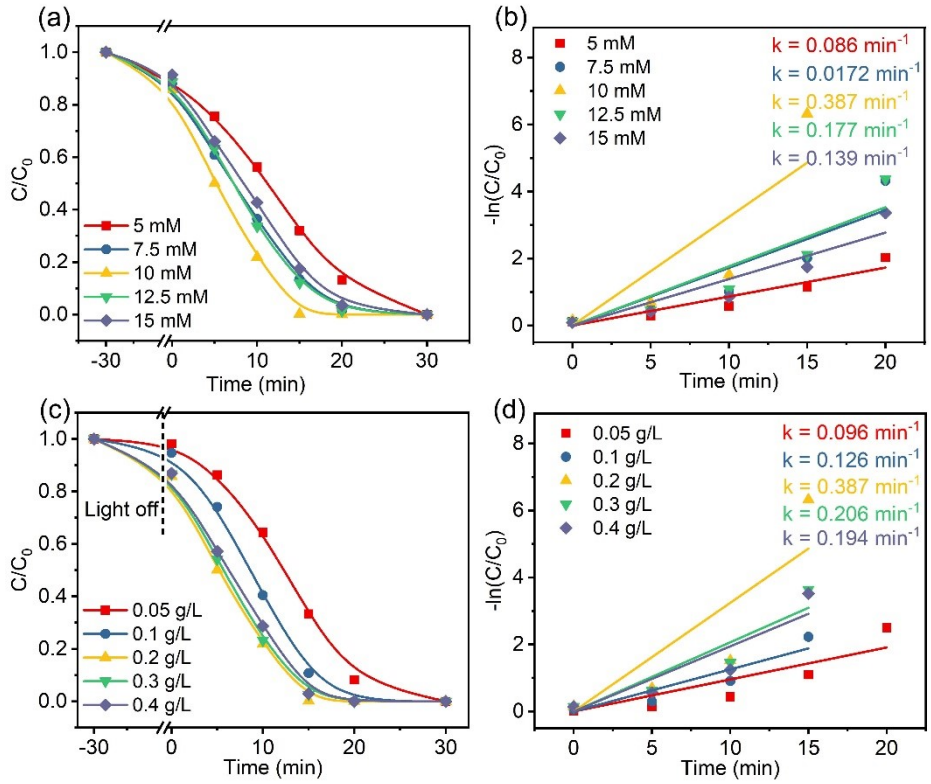

Fig. S8 Effects of (a) H_2O_2 concentration and (b) corresponding *k* value on phenol removal over Cu^0@CuZ. (c) catalyst dosage and (d) corresponding *k* value on phenol removal over Cu^0@CuZ.

As depicted in Figs. S6a-b, the phenol removal efficiency increased from 87% to 100% when H_2O_2 concentration raised from 5 to10 mM, and the k value of Cu^0@CuZ markedly increased from 0.086 to 0.387 min^{-1}, which was due to the increasing concentration of H_2O_2 can produce more •OH for phenol removal. However, both the removal efficiency and the k value decreased as the H_2O_2 concentration further increased to 15 mM, which is due to the fact that the excessive H_2O_2 could be a scavenger for •OH (An 2023). Therefore, 10 mM H_2O_2 was selected as the optimum reaction parameters. The catalyst dosage influence on phenol removal efficiency was exhibited in Figs. S6c-d. When the Cu^0@CuZ dosage was greater than 0.1 g/L, 100% phenol removal efficiency was achieved. Notably, the k value increased from 0.096 to 0.387 min^{-1} with an increase in catalyst dosage from 0.05 to 0.2 g/L, which is owing to that the higher catalyst dosage produces the more H_2O_2 activation sites to generate more •OH, leading to the good phenol removal efficiency. Nevertheless, with further increasing of Cu^0@CuZ dosage from 0.2 to 0.4 g/L led the k value decreased. This is mainly attributed to that the superfluous catalysts could reduce the solution transmittance, resulting in light scattering, and the sum total of photons eventually reaching the surface of catalyst would be reduced.

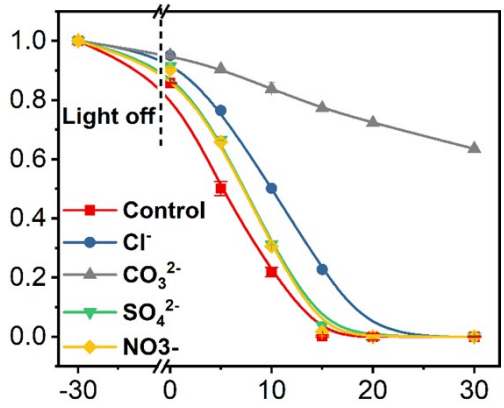

Fig. S9 Effects of coexisting anions on phenol removal efficiency over Cu^0@CuZ.

The addition of CO_3^{2-} inhibited the phenol removal efficiency by 63%. The reasons for the decrease are as follows: CO_3^{2-}, as trapping agent for •OH, would react with •OH to generate $•CO_3^-$ with weak oxidation ability; CO_3^{2-} in the water bodies can easily form HCO_3^-, OH^-, and H_2CO_3, leading to an increase in reaction system pH value (Eqs. 1−3), and the catalytic activity of the Cu^0@CuZ would be hindered.

$$CO_3^{2-} + •OH \rightarrow •CO_3^- + OH \quad (1)$$

$$CO_3^{2-} + H_2O \rightarrow HCO_3^- + OH^- \quad (2)$$

$$HCO_3^- + H_2O \rightarrow H_2CO_3 + OH^- \quad (3)$$

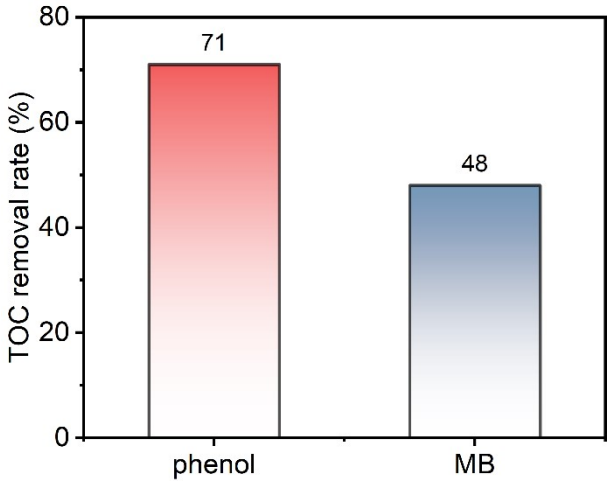

Fig. S10 The TOC removal rate of phenol and MB over Cu^0@CuZ in photo-Fenton-like system within 90 min.

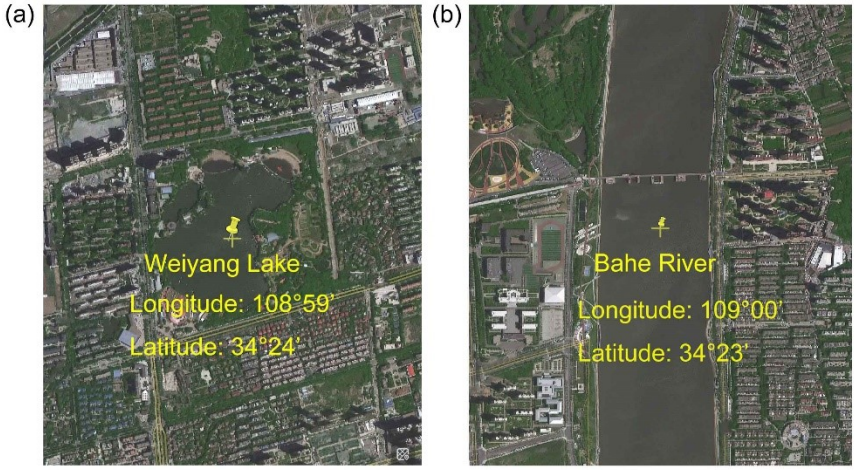

Fig. S11 (a) Lake water and (b) river water intake point.

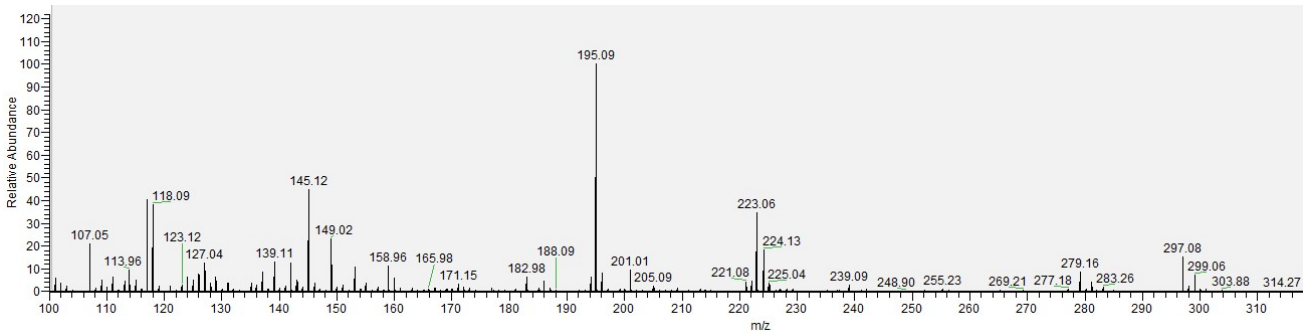

Fig. S12 Mass spectrum peak obtained from the DCF degradation over Cu^0@CuZ after 10 min irradiation.

References

1. M. Frisch, G. Trucks, H. Schlegel, G. Scuseria, M. Robb, J. Cheeseman, G. Scalmani, V. Barone, G. Petersson and H. Nakatsuji, Gaussian, Inc., Wallingford CT, 2016, *Gaussian09, Revision D*, 20 16, **1**.
2. T. Lu and F. Chen, Multiwfn: a multifunctional wavefunction analyzer, *J. Comput. Chem.*, 2012, **33**, 580-592.
3. T. Lu and Q. Chen, in *Conceptual Density Functional Theory*, 2022, DOI: 10.1002/978352782994 1.ch31, pp. 631-647.
4. R. G. Parr and W. T. Yang, Density Functional-Approach to the Frontier-Electron Theory of Che mical-Reactivity, *J. Am. Chem. Soc.*, 1984, **106**, 4049-4050.
5. J. Hu, J. Li, J. Cui, W. An, L. Liu, Y. Liang and W. Cui, Surface oxygen vacancies enriched F eOOH/Bi_2MoO_6 photocatalysis-Fenton synergy degradation of organic pollutants, *J. Hazard. Mater.*, 2020, **384**, 121399.
6. L. Yu, J. Chen, Z. Liang, W. Xu, L. Chen and D. Ye, Degradation of phenol using Fe_3O_4-GO n anocomposite as a heterogeneous photo-Fenton catalyst, *Sep. Purif. Technol.*, 2016, **171**, 80–87.
7. X. Qian, Y. Wu, M. Kan, M. Fang, D. Yue, J. Zeng and Y. Zhao, FeOOH quantum dots couple d g-C_3N_4 for visible light driving photo-Fenton degradation of organic pollutants, *Appl. Catal. B*, 2018, **237**, 513–520.
8. A. Fiorentino, R. Cucciniello, A. Di Cesare, D. Fontaneto, P. Prete, L. Rizzo, G. Corno and A. Proto, Disinfection of urban wastewater by a new photo-Fenton like process using Cu-iminodisucci nic acid complex as catalyst at neutral pH, *Water Res.*, 2018, **146**, 206-215.
9. P. K. Boruah, B. Sharma, I. Karbhal, M. V. Shelke and M. R. Das, Ammonia-modified graphene sheets decorated with magnetic Fe_3O_4 nanoparticles for the photocatalytic and photo-Fenton degrad ation of phenolic compounds under sunlight irradiation, *J. Hazard. Mater.*, 2017, **325**, 90-100.
10. P. Garcia-Muñoz, F. Fresno, C. Lefevre, D. Robert and N. Keller, Highly robust $La_{1-x}Ti_xFeO_3$ dua l catalyst with combined photocatalytic and photo-CWPO activity under visible light for 4-chlorop henol removal in water, *Appl. Catal. B*, 2020, **262**, 118310.
11. Z. Zhao, X. Cai, S. Fan, Y. Zhang, Z. Huang, H. Hu, J. Liang and Y. Qin, Construction of a st able Cu-Fe@C composite catalyst with enhanced performance and recyclability for visible-light-dri ven photo-Fenton reaction, *J. Alloys Compd.*, 2021, **877**, 160260.
12. Y. Li, X. Wang, Z. Duan, D. Yu, Q. Wang, D. Ji and W. Liu, Zn/Co-ZIFs@MIL-101(Fe) metal-organic frameworks are effective photo-Fenton catalysts for RhB removal, *Sep. Purif. Technol.*, 20 22, **293**, 121099.
13. M. Liu, H. Xia, W. Yang, X. Liu, J. Xiang, X. Wang, L. Hu and F. Lu, Novel Cu-Fe Bi-metal oxide quantum dots coupled g-C_3N_4 nanosheets with H_2O_2 adsorption-activation trade-off for effici ent photo-Fenton catalysis, *Appl. Catal. B*, 2022, **301**, 120765.
14. A. Corma, V. Fornes, S. B. Pergher, T. L. M. Maesen and J. G. Buglass, Delaminated zeolite pr ecursors as selective acidic catalysts, *Nature*, 1998, **396**, 353-356.

15. H.-K. Min, S. Kweon, S. Oh, H. An, Y. Cho, H. Min, D. Jo, J. F. Kim, C.-H. Shin, S. B. Kang and M. B. Park, Single-step preparation of zinco- and aluminosilicate delaminated MWW layers f or the catalytic conversion of glucose, *Green Chem.*, 2021, **23**, 9489-9501.
16. L. Singh, P. Rekha and S. Chand, Cu-impregnated zeolite Y as highly active and stable heterogen eous Fenton-like catalyst for degradation of Congo red dye, *Sep. Purif. Technol.*, 2016, **170**, 321-336.